# Conjugated and Redox Polymer Composites for Organic Electrochemical Energy Storage Electrodes

By

Danny Illera Perozo

A dissertation submitted in partial fulfillment of the requirements for the
degree of
Doctor of Philosophy
Department of Mechanical Engineering
Universidad del Norte
Barranquilla-Colombia

Major Professor:
Humberto Gomez Vega, Ph.D.
Committee Members:
Antonio Bula, Ph.D.
D. Yogi Goswami, Ph.D.
Julio Mass Varela, Ph.D.
Pedro Villalba Amaris, Ph.D.

May 2019

## Acknowledgments

Special thanks are due to my advisor Humberto Gomez for his counseling, patience, understanding, encouragement, constructive criticism and willingness to share his expertise as he directs me in my studies and future endeavors. I would also like to thank the members of my doctoral committee, Dr. Antonio Bula, Dr. Yogi Goswami, Dr. Julio Mass, and Dr. Pedro Villalba; for their invaluable support and guidance during the development of this dissertation. Thanks also to the Centro Integrado de Materiales y Manufactura (CIMM) staff at Universidad del Norte, in particular to Luis Ruiz for his disposition and enthusiasm while assisting my experimental work.

I am also really grateful for the warm reception and assistance provided by the Clean Energy Research Center (CERC) team at the University of South Florida during my doctoral internship. Particularly to Dr. Yogi Goswami for his kindness and giving me the opportunity to be part of the CERC group while openly sharing his expertise and priceless suggestions.

And last but not least, this work is devoted to my family, my parents Alicia and Pedro and my girlfriend Cinthia, for their endless love that helped me to go throughout this whole process.

# Table of Contents

# 1 Background and Motivation

Widespread growth of energy storage technologies comes hand in hand with the penetration of renewable energy sources and the proliferation of electric transportation technologies. Although Electrochemical Energy Storage (EES) is forecasted as key player for integration of the aforementioned technologies, current device production lacks of a *sustainable* approach. For instance, around 328 kWh of energy is required and 110 kg of $CO_2$ is released in order to build a lithium-ion battery capable of storing/delivering 1 kWh [1]. On the other hand, around 1 kg of $CO_2$ is released when 1 kWh of energy is produced from direct coal combustion. Further, conventional cathode materials are based on non-renewable transition metal oxides or phosphates ($LiCoO_2$, $LiMn_2O_4$, $LiFePO_4$, among others). Waste flows from projected electric vehicle use concludes that only 42% of the total waste by mass can be recycled with current technology [2]. There is also concerns regarding the limited Li resources, the uneven distribution of such resources, and the increasing cost of the metal [3], [4]. The challenge is thus the fabrication of EES devices that meet current and future performance requirements while following *sustainable* protocols and exploiting *renewable* materials.

The former challenge suggests the incorporation of low-cost, abundant and renewable electroactive materials produced by low energy demand and low carbon fingerprint routes [5], [6]. Particularly, one can identify a set of basic criteria according to the discussion given by Larcher and Tarascon [6] as well as the green chemistry and engineering principles suggested by Anastas & Warner [7] and Anastas & Zimmerman [8] (refer to Table 1). However, other application-oriented criteria regarding system integration, operation, maintenance and disposal must be kept in mind. This leads to the twelve-principles for the design and application of green energy storage for the grid, developed by Arbabzadeh and coworkers [9]. Overall, a set of basic criteria towards sustainable EES system design and production is identified based on the aforementioned discussions. The first principle

dictates de use of ready available and renewable chemical precursors. The availability of chemical precursors is dictated by an interplay between abundance, market and geopolitics [10]. In this regard, bio-based feedstocks accomplish the aforementioned criteria. A key point to bear in mind is that the sole incorporation of "bio-based materials" into electrochemical energy storage technologies does not guarantee an improvement in terms of sustainability. Tools like a life-cycle assessment should be used to convey an objective criterion for comparison. The availability of chemical precursors by itself is as critical as the steps necessary to transform such raw materials in order to meet the requirements for a specific technological application. Materials processing account more than half of the energy demand of industrial processes and industrial processes by itself accounts more than one quarter of world energy demand [11].

Table 1 The 12 principles of Green engineering according to Anastas & Zimmerman [8]

**12 Principles of Green Engineering**

| | |
|---|---|
| 1 | Designers need to strive to ensure that all material and energy inputs and outputs are as inherently nonhazardous as possible. |
| 2 | It is better to prevent waste than to treat or clean up waste after it is formed. |
| 3 | Separation and purification operations should be designed to minimize energy consumption and materials use. |
| 4 | Products, processes, and systems should be designed to maximize mass, energy, space, and time efficiency. |
| 5 | Products, processes, and systems should be "output pulled" rather than "input pushed" through the use of energy and materials. |
| 6 | Embedded entropy and complexity must be viewed as an investment when making design choices on recycle, reuse, or beneficial disposition. |
| 7 | Targeted durability, not immortality, should be a design goal. |
| 8 | Design for unnecessary capacity or capability (e.g., "one size fits all") solutions should be considered a design flaw. |
| 9 | Material diversity in multicomponent products should be minimized to promote disassembly and value retention. |
| 10 | Design of products, processes, and systems must include integration and interconnectivity with available energy and materials flows. |
| 11 | Products, processes, and systems should be designed for performance in a commercial "afterlife". |
| 12 | Material and energy inputs should be renewable rather than depleting. |

Table 2 Design Oriented Principles for Green Energy Storage Systems according to Arbabzadeh and coworkers [9]

| | Design Oriented Principles for Green Energy Storage Systems |
|---|---|
| 1 | Minimize consumptive use of non-renewable materials. |
| 2 | Minimize use of critical materials. |
| 3 | Substitute non-toxic and non-hazardous materials. |
| 4 | Minimize the environmental impact per unit of energy service for material production and processing. |
| 5 | Design for end-of-life. |

# 2 Polymer-Based Electrochemical Energy Storage

## 2.1 Introduction

Regarding the need for sustainable production of EES technologies, polymers offers certain advantages over traditional inorganic compounds:

- Adjustable redox potential with the addition/removal of functional groups to the main chain.

- Constituted of abundant elements (such as C, H, O, N, and S, among others).

- Compatible not only with traditional Li-ion chemistry, but also with beyond-Li technologies such as Na, Mg or Zn because its electro-activity relies mainly on conversion reactions.

However, although the Steel and Cement production accounts for roughly the 50% of the annual energy use for material production (refer to Figure 1a), the energy intensity required to produce a material from its raw form per unit mass (embodied energy) is actually higher for polymers (refer to Figure 1b). This represent a drawback if massification of polymer use for sustainable EES technologies is desired.
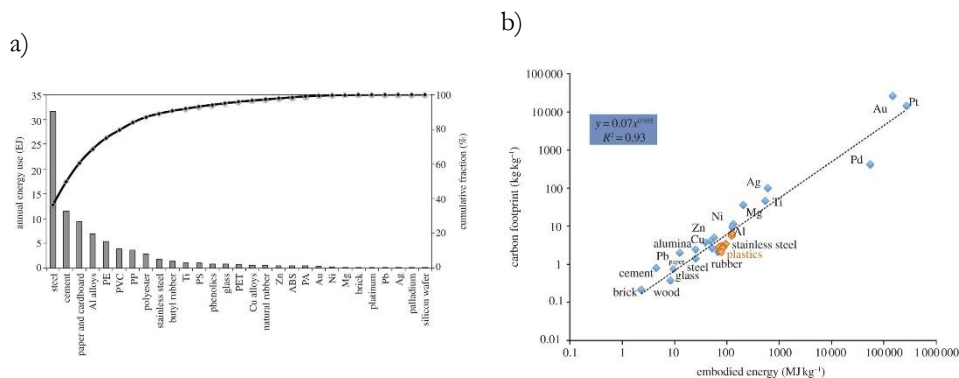


Figure 1 a) Annual primary energy used for the production of selected materials worldwide, b) The carbon fingerprint per kilogram of material produced versus the embodied energy (Reproduced without permission from [12])

Traditionally it is also often stated that the main technical challenges facing electro-active polymers for EES electrodes include:

➢ High solubility in common organic-based electrolytes leading to self-discharge and low cycling stability.

➢ Low electronic conductivity

Therefore, a study is carried out in order to identify the current role of polymers in the field of EES. The goal is to specifically identify the trends and challenges regarding electro-active polymers for battery and electrochemical capacitor related applications.

### 2.1.1 Methodology

A bibliometric analysis is performed in order to identify the main research trends regarding polymer-based electrochemical storage. The corresponding analysis involves the following steps:

▪ Data Acquisition: Data is retrieved from Web of Science database. A search is performed using the terms "Electrochemical Energy Storage" and "Polymer/Polymers" as topics. The initial search is meant to be as wide as possible to avoid any bias. The timespan is set to the last 5 years.

▪ Data Processing: The document types are refined to consider only articles. The Bradford's law is used in order to identify and further consider the top core journals.

▪ Data Analysis: The keywords (author and keyword plus) of the resulting articles are used to create a co-occurrence bibliometric network. The keywords are previously homogenized taking into consideration synonyms (such as "supercapacitor" and "electrochemical capacitor") and eliminating meaningless terms (e.g. "material", "performance", "properties", among

others). A distance-based approach is used based on the work by Van Eck & Waltman [13].

## 2.2 Results of Bibliometric Analysis

After performing the initial search according to the Data Acquisition step described previously in 2.1.1 a total of 2433 articles are retrieved. The Bradford's law is used as a way to identify the "core" journals. The Bradford's law for scientometrics states that articles in a given discipline are concentrated in a relative small number of journals central to the discipline [14]. Those "core" journal are considered to be the ones where significant research advances are published. Therefore, the initial search is refined in order to screen those articles that belong to the following journals: Electrochimica Acta, Journal of Materials Chemistry A, ACS Applied Materials & Interfaces, RSC Advances, Journal of Power Sources and Nanoscale. The total number of articles studied after journal screening is 784.



Figure 2 Network Map for the Co-Occurrence Analysis. The gray key-words correspond to terms without cluster association.
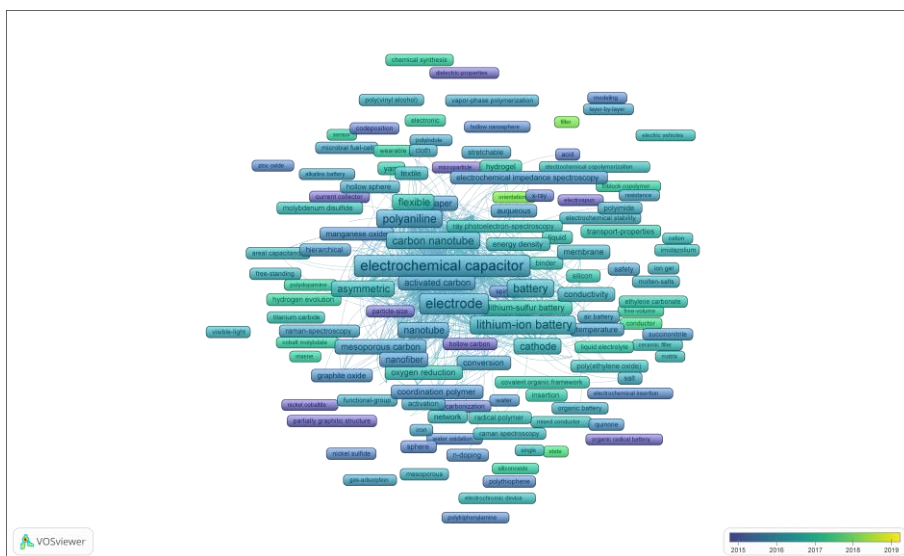
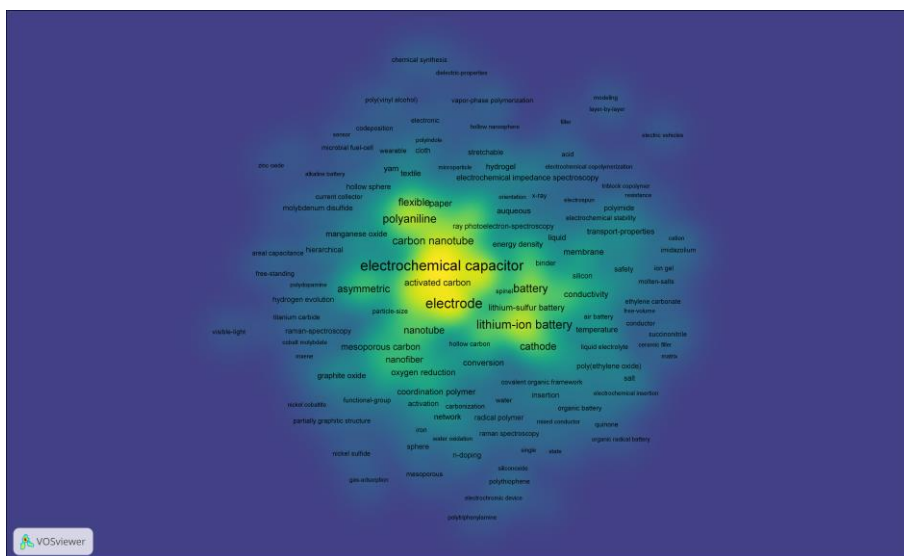Figure 3 Network Map for the Co-Occurrence Analysis.



Figure 4 Density Map for the Co-Occurrence Analysis.

The keywords are extracted from the selected papers and further analyzed (refer to Figure 2, Figure 3 and Figure 4). Clustering of keywords allows mapping well-stablished research trends. Cluster refinement is performed until reaching a constant number of groups. The purpose of gathering a large number of clusters is to set aside high-frequency keywords that will eventually not belong to any cluster. Therefore, the clusters are expected

to be formed by low- to mid-frequency keywords which have shown to provide the highest discrimination degree [15]. A total of 49 clusters were obtained. These clusters were further refined to a total of 22 clusters discarding those who contained a group of meaningless terms for the purpose of research trend identification (refer to Figure 5). Each cluster is then analyzed exploring its top articles and the research field is constructed identifying its goals and challenges. Within each cluster, top articles are selected based on its corresponding number of citations. This allows to create a description of main challenges for the research field. More recent articles are then reviewed in order to identify explored solutions and their effectiveness.
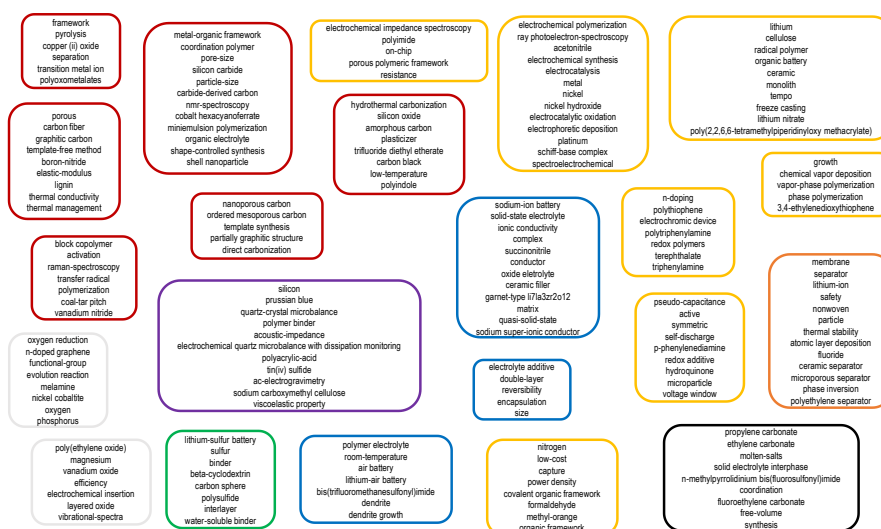
Figure 5 Clustering of Keywords

The clusters are further grouped into 7 categories according to the role of the polymeric material. The categories identified are:

- Polymers as precursors or sacrificial templates for the formation/synthesis of Carbon/Metal/Metal-Oxide Micro- and Nano-Porous Structures.

- Polymers as Electroactive Materials for Electrochemical Storage Electrodes.

- Polymers as Mechanical Properties Enhancers for Nonwovens Separators.

- Polymers as Gelators for Solid Polymer Electrolyte formation by Immobilization and Encapsulation of Room-Temperature-Ionic-Liquids/Ceramics.

- Polymers as Mechanical Properties Enhancers for the Solid-Electrolyte-Interphase (SEI).

- Polymers as Spacers to prevent agglomeration and stacking of 2D Energy Storage Materials.

- Polymers as Immobilization agents for Sulfur in Li-S Batteries.

Among those, it is further studied the category corresponding to "Polymers as Electroactive Materials for Electrochemical Storage Electrodes" as this is the only category exploiting the inherent charge storage of polymeric materials. In what follows, each cluster belonging to the aforementioned category is analyzed identifying its goals and challenges.

## 2.3 Overview of Electro-Active Polymer Research for EES

Electro-active polymers store charge by performing reversible redox reactions. Different schemes have been proposed in order to classify electro-active polymers. One common scheme is precisely associated with the state of charge of the polymer upon "charging": n-type, p-type or bipolar. An n-type polymer is charged by accepting electrons resulting in a negative charge state. On the other hand, a p-type is charged upon electron removal resulting in a positive charge state. Within the bipolar category lies those polymers able to be charged either by an n- or p-type process.

Most importantly is identifying the redox potential necessary to carry on the reaction. This will dictate the suitable role of polymer material either as cathode or anode in an EES device (refer to Figure 6). Regarding theoretical capacity, it is noticeable that low molecular weight carbonyl derivatives (such as benzoquinone) could reach a theoretical capacity of ~500 mAh g$^{-1}$.
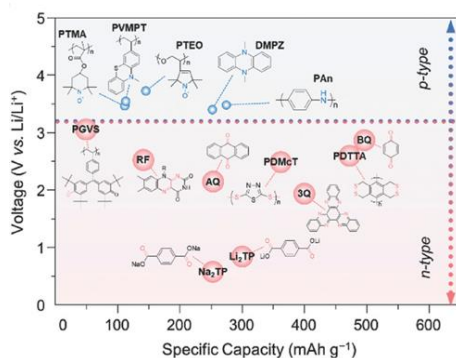
Figure 6 Redox potential vs. theoretical capacity of selected organic compounds. Reproduced without authorization from [16]

### 2.3.1 Freeze-Casting of Porous Organic Electrodes

Electrode porosity have a significant influence on electrochemical performance. In principle, a porous morphology is pursued in order to enhance ion diffusion and thus rate capability of the electrode. Most of the studies carried out in this regard reported random pore structures making difficult to offer a fair comparison. Very few studies like the one performed by Stolze and coworkers [17] obtained defined pore geometries. Ice-templating (or freeze-casting) allowed the construction of columnar and parallel pores with controllable diameter. Comparison with a traditional "planar" electrode revealed that the rate capability was actually lower for the porous electrode. That behavior was attributed to the significantly larger thickness of porous electrodes in combination with their lower electronic conductivity.

### 2.3.2 Conjugated Polymer Nanocomposites

Ternary composites of conjugated polymers with pseudocapacitive transition metal (such as $MnO_2$) and carbon nanostructures are developed seeking a synergic increase in the capacitance relative to the individual components [18]–[20]. The main drawback with such composites/hybrids is their low rate capability and cyclic stability at high currents. This

could be explained by the fact that the typical interaction between polymer and additives involves secondary bonding which may not be strong enough to withstand the volumetric changes of the polymer during charging/discharging. Primary bonding (i.e. covalent linking) is not desired in most of the cases to avoid disruption of the conjugated polymer backbone.

### 2.3.3    Conjugated Polymers with Redox Active Pendent Groups

The incorporation or anchoring of redox active pendent functional groups to a CP backbone allows the simultaneous exploitation of the intrinsic conductivity of the backbone and the charge capacity of the pendant group potentially eliminating the need of adding non-active conducting additives. Obtaining redox potential matching between the CP backbone and the redox group is a key factor in realizing such concept.

In this regard, terephthalate undergo two redox processes resulting in a reversible capacity up to 300 mAh $g^{-1}$ [21]. These compounds could be synthesized from biomass and recycled. Therefore, terephthalate-polythiophenes compounds were synthesized following an electro-polymerization protocol [22], [23].

### 2.3.4    Aromatic Polyimides Porous Polymeric Frameworks

Aromatic Polyimides highlights with a theoretical capacity close to 400 mAh $g^{-1}$. Its electro-activity is mainly based on the reduction of carbonyl groups derived from dianhydrides involving two reversible one-electron steps to yield the anion radical and the dianion.

In order to avoid dissolution of the polymer into the electrolyte, porous organic frameworks on carbon nanostructures have been constructed. This approach is preferred because it allows the simultaneous polymerization and formation of a porous morphology necessary for ionic species fast diffusion. However, the specific capacities follows an inverse

proportion to the molecular weight of the polymeric framework, limiting the capacities close to 150 mAh g$^{-1}$.

### 2.3.5 Incorporation of Schiff Base Complexes into Polymers

A Schiff Base could be depicted as an aldehyde- or ketone-like compound in which the carbonyl group is replaced by an azomethine (-R=CN-) group. Transition Metal (M) complexes with Schiff Bases, known as poly[M(Schiff)] or metal-salen type polymers, are particularly attractive for EES because of its wide potential window, reversible redox behavior, thermal stability up to 350°C and high electronic conductivity.

PolyNi(salphen), polyNi(CH$_3$-salphen), and polyNi(CH$_3$O-salphen) have been proposed as electrode material for electrochemical capacitors [24]–[27]. It is pointed out that the low solubility of these complexes and the limited synthetic routes for obtaining polymerizable monomers have delayed further progress for EES applications.

## 2.4 Main Findings regarding Electro-Active Polymer Research for EES

The following conclusions could be drawn regarding the application of polymers for electrochemical storage electrode fabrication:

- The incorporation of **conducting additives** (up to 60% of electrode mass) is necessary for improving the inherent **low electronic conductivity** of most polymer electro-active materials. Even intrinsic conducting polymers based electrodes seem to benefit from the increased conductivity, although requiring less additive load. The main drawback is the significant **reduction in the specific capacity** of the electrodes due to the addition of non-electro-active mass.

- **Larger surface area** makes ions more accessible to active material improving the diffusion rate during the cycle; however, it also promotes **dissolution** of

the polymeric material. The increased diffusion length of a proper **open porous structure** (such as a foam or aerogel) could even **decrease the rate capability** of the electrode.

- Although **polymerization** have shown to **improve** significantly the **dissolution** problem of organic-based electrodes, it generally leads to a **reduction in the specific capacity**. This is because it is often necessary to add pendant groups to the monomer that work as connecting links during polymerization. The additional non-active mass leads to a reduction of the specific capacity. Also, the typical resulting polymer is **non-conductive decreasing rate performance**.

- Substitution of **metal cations** affects the crystal structure of the polymer. **Dissolution** could be **decreased** by strengthening the inter-chain interaction when combining highly electronegative atoms located in the polymer chains (F, Cl among others) with metal cations.

- Adding **substitute functional groups** to the polymer allows **redox potential** tuning. However, the increased **molecular weight** diminish the **specific capacity** of the resultant material.

- Increasing the **conjugation length** of the polymer provides a backbone for charge carrier movement, thus theoretically increasing the conductivity of the polymer. Addition of bulky substitute functional groups should be avoided in order to reach conjugation between monomer units.

# 3 Research Objectives and Approach

Previous chapters identified the main challenges for improvement of polymer electrochemical performance and highlighted the need for a more sustainable production of the same. However, it is noticeable the lack of approaches to address both requirements at

the same time. Therefore, the scope of this thesis is to define and test a set of strategies to simultaneously improve the aforementioned needs during design and synthesis of different polymer-based materials for EES. To do so, first a set of rules for material design and synthesis have been defined highly influenced from the 12 Principles of Green Engineering [8]:

- **Solution-based synthesis of polymers in an aqueous media.** Solution-base approaches are attractive for its industrial scalability. An aqueous media is preferred for its low toxicity.

- **Substitution of organic electrolyte for an aqueous electrolyte.** This aims toward reducing solubility of organic materials and simultaneously decrease toxicity of the device.

- **Incorporation of low-cost commercial available materials.**

From an electrochemical performance perspective, the following measures have been followed:

- **Polymerization** of **high specific capacity organic molecules** (i.e. benzoquinone) without the need of adding anchoring functional groups to the monomer, in order avoid a decrease of specific capacity due to the additional inactive mass.

- Promote the formation of **core-shell structures** constituted of polymer layers deposited in high aspect ratio carbon nanostructures (i.e. graphene). The idea is to reduce the amount of conducting additive to be added to the electrode by increasing the contact area between polymers and conducting phase. In this regard, core-shell formation also have a **nano-templating** effect, here understood as the use of nanostructures to control de morphology of the polymer. Therefore, addition of high aspect ratio nanostructures enhances in principle the formation of a more open electrode morphology.

18

One critical step here is avoid the **intrinsic agglomeration** of **high aspect ratio nanostructures** during polymer synthesis.

- Related with the previous measure, the **mass ratio** of the added **nanostructures** is maintained below 0.15 accepting a maximum reduction in the theoretical capacity of the composite of the same magnitude.

- **Aerogel** or **foam** formation is **avoided** as studies reveal that such open porous structure could actually decrease the rate capability of the electrodes due the reduction of contact between solid-phase and the increase in diffusion length due to its larger thickness compared to traditional "2D electrodes".

- **Cross-linking** of polymer post electrode formation is explored as a strategy to reduce dissolution and diffusion path collapse upon cycling.

Based on all the aforementioned, two specific monomers have been targeted: **aniline** and **benzoquinone**. Aniline is chosen due to its moderate specific capacity (288 mAh $g^{-1}$) but high theoretical capacitance once polymerized (964 F $g^{-1}$). Thus, it is oriented to capacitive-like storage. On the other hand, benzoquinone highlights for its high theoretical capacity (496 mAh $g^{-1}$) but low electronic conductivity compared to aniline. Therefore, it is oriented to battery-like storage.

Despite current production of the selected monomers is mostly derived from the petrochemical industry, there are new insights into the bio-based production of the same [28], [29], targeting to the sustainability measures previously described.

# 4 Polyaniline Core-Shell Structures with Diamond Nanoparticles and Graphene*

## 4.1 Background

High volume and low cost synthesis of customizable polymer-based electro-active materials holds the key to their widespread commercialization in electrochemical energy storage technologies. Considering specifically electrochemical capacitor (also known as *supercapacitor*) electrodes, conjugated electro-active polymers (CEP) would be a cheaper, lighter and more efficient solution than toxic and scarce transition metal oxides or limited-capacitance high surface-area activated carbons. In order to accomplish excel electrochemical performance compared to the aforementioned candidates it is mandatory to control the morphology, specific surface-area, electronic/ionic conductivities and electrochemical stability CEP electrodes.

High surface-area CEP are generally achieved by template-assisted and template-free synthesis of nanostructured polymers [30]. As a representative example, hollow polyaniline electrospun nanofibers reported almost a threefold increase in charge storage capacity relative to conventional compact polyaniline powder [31]. However, nano-structuring has a minor impact on the long-term electrochemical stability of the electrodes. Charge transfer and charge transport on polymer film electrodes involves incorporation/release of electrolyte ions and solvent molecules. Therefore, charge storage cycles implies swelling and shrinkage of the film that might lead to irreversible changes like dissolution of polymer chains as the main cause of electrode performance degradation [32].

Covalent and non-covalent anchoring of CEP chains to an electrochemically stable support not only provides a measure against dissolution related degradation, but also an

---

*Disclaimer: Contents of this chapter have been submitted for publication in a refereed journal.

opportunity to exploit micro/nano-composite effects. Among CEP and micro/nano substrate possible combinations, polyaniline (PANI) and graphene (G) hybrids have been considerably studied over the past five years boosted for the reported enhancements on the electrochemical performance. In terms of charge storage and transport properties, the improvements lies within a range of 1 to 10 times the corresponding behavior of PANI [33]–[40]. The wide range of reported values seems to be a consequence of the structure, composition, mass and thickness of the final PANI/G thin-film electrode. The electrode composition plays an interesting role as different proportions of insulating binders are commonly used to facilitate the formation and stability of PANI/G thin-films. Many reports reveal that specific charge storage capacity is calculated using small electrode mass or thickness, leading to possible over-estimations.

The intrinsic morphology of the thin-film is a direct consequence of the polymer-based nano-composite synthesis technique. In this regard, template-assisted techniques provide good morphological control. A template removal step would distort the original structure [41], [42], so a more efficient approach would be to use a permanent template that also adds new features beyond morphology control. Graphene outstands as a template due to its large specific surface-area (2675 m²/g) that is only accessible as long as the high tendency to individual sheet restack is prevented. The high electrical conductivity of graphene is desired in order to boost the PANI/G charge transfer kinetics. Nano-diamond particles (particularly, detonation nano-diamond particles) highlight with large specific surface-area, tunable surface chemistry, and cheap synthesis compared to its bulk counterpart [43]. For Electrochemical Energy Storage (EES) applications diamond offers a high potential window (e. g. ~7.0 in non-aqueous electrolytes) [44] and chemical stability. Therefore, proper exploitation of this material could lead toward an increase of the cycle life of related devices and, for the particular case of electrochemical capacitors, an increase of the energy density of the device which is proportional to the square of the operating voltage. Furthermore,

contrary to its bulk counterpart, diamond nanoparticles manifest improved electronic conductivity and redox activity as well as high surface area [45]. In contrast to graphene, nano-diamond has been scarcely studied for polymer-based energy storage applications although results are promising. Briefly, it has been reported a redox activity at wider potential windows (e.g. 3500 mV for P/ND vs. 1000 mV for pure PANI) [46] and even a charge storage capacity retention of ~120% after 10000 charge/discharge cycles [47]. Nano-diamond particles seems to contribute significantly on the polymer-based nanocomposite stability. Evidence suggests that only the diamond surface is electrochemically active during the time scale of measurements (i.e. the internal structure of diamond is not accessible for the purpose of energy storage). Therefore, the size of diamond particles should be minimized and kept isolated for efficient exploitation of this material.

Commercial grade graphene is typically synthetized from chemical/thermal exfoliation and reduction of graphite oxide and sold as "powders" or dispersions [48]. Similarly, commercial nano-diamond is also sold as powders or dispersions, produced by detonation of discarded explosives in an oxygen deficient atmosphere [43]. A rational approach, as proposed herein, towards high volume synthesis of polymer-infiltrated nano-sheets and nano-particles would be a scalable solution-based method able to disperse and de-agglomerate G and ND clusters. The final aim is to assess and advance the development of cost-effective polymer-based energy storage materials through a processing-structure-property interrelationship discussion for scalable synthesis methods.

## 4.2 Experimental Procedure

### 4.2.1 Materials and Reagents

Unless otherwise stated, the chemicals were ACS quality and used as received without further purification. Pristine graphene powder had a thickness between 50-100 nm, x-y

dimensions close to ~5 μm and a carbon content of ~97.0%. Detonation nanodiamond had an average particle size of ~4.0 nm and ~98.0% purity.

### 4.2.2 Synthesis of PANI/G/ND

The aniline (AN) to G and to ND mass ratios were varied between 0% − 20% and 0% − 10%, respectively. For each case, AN (0.2M), G and ND were mixed in a 1M HCl solution. The mixture was placed in an ice bath and homogenized by magnetic stirring for 15 minutes. A solution of 0.05M $(NH4)2S2O8$ in 1M HCl was then added dropwise. After 48 hours of reaction and continuous stirring, a dark green precipitate was obtained at the bottom of the flask. The precipitate was filtered and washed with deionized water, methanol, isopropyl alcohol and acetone. The precipitate was then dried in an oven at 85°C for 6 hours. Finally, the resulting material were immersed in a 2M $NH_4OH$ solution for 24 hours, then filtered, washed and dried as described above. Each sample is labeled as XXG − YYND, where XX and YY represents the G/AN and ND/AN mass fraction percentage, respectively.

### 4.2.3 Material Characterization

For FTIR spectroscopy, the samples were prepared following the KBr pellet method and the spectra recorded on a Shimadzu IR Prestige-21 Spectrometer (Transmittance Mode). Thermal analyses were carried out recording simultaneously the TGA and DSC profiles using a STD-Q600 TGA/DSC (Scan Rate: 20°C/min, Atmosphere: Ar, Temperature Range: 25°C - 600°C). For electron microscopy, the specimen preparation were carried out by drop casting (50 μL), on Indium Tin Oxide (ITO) coated glass or copper grid 300 mesh, a dispersion of the composite in N,N-Dimethylformamide (15 mg/mL). SEM and TEM observations were performed in a Jeol JSM 5600 and a Tecnai G2 20, respectively.

For electrochemical characterization, each electrode was prepared by mixing the active material, carbon black (conductive agent) and nafion (binder) maintaining the following mass proportion 70:20:10. A nafion dispersion (10% wt. in water/alcohol) is diluted first in isopropyl alcohol. Carbon black is then added to the dispersion followed by the active material. The slurry is casted on ITO glass by the doctor blade technique. The electrodes are dried at 75°C for 6 hours and then at 150°C for 3 hours. The electrodes are immersed overnight in the electrolyte previous electrochemical measurements. All electrochemical tests were perfomed using a 0.1M solution of $LiClO_4$ dissolved in acetonitrile as electrolyte and a three electrode set-up consisting of polymer-modified electrode as working electrode, Saturated Calomel Electrode (SCE) as reference electrode and a graphite rod as counter electrode.

## 4.3   Material Characterization and Analysis

Figure 7 shows the FTIR spectra of all the synthesized nanocomposites. Except for the $10G - 10ND$ and $20G - 10ND$ cases, it can be identified a group of peaks at positions ~1585.5 cm-1, ~1498.7 cm-1, ~1375.3 cm-1, ~1309.7 cm-1, ~1244.1 cm-1, ~1165.0 cm-1 and ~829.4 cm-1. These peaks correspond to the modes of vibration of $\nu Q$, $\nu B$, $\delta$(C-N) [QBQ], $\nu$(CN) [Secondary Amine], $\nu$(C-N) [BBB], N=Q=N/$\delta$(C-H) and $\Upsilon$(C−H) groups, respectively, indicating the presence of polyaniline in emeraldine base state [49], [50]. For ND containing samples, the broad absorption peak between ~3750 cm-1 and ~3000 cm-1 is from the OH and NH groups on ND surface [51]. For the $10G - 10ND$ sample, the peaks at positions ~1735.9 cm-1, ~1365.6 cm-1, ~1220.9 cm-1 and ~987.6 cm-1 can be associated to the modes of vibration of C=O, C-OH, C-O (Epoxy) and C-O (Alkoxy), respectively [49]. These peaks also appear in the $0G - 10ND$ spectra with less intensity.
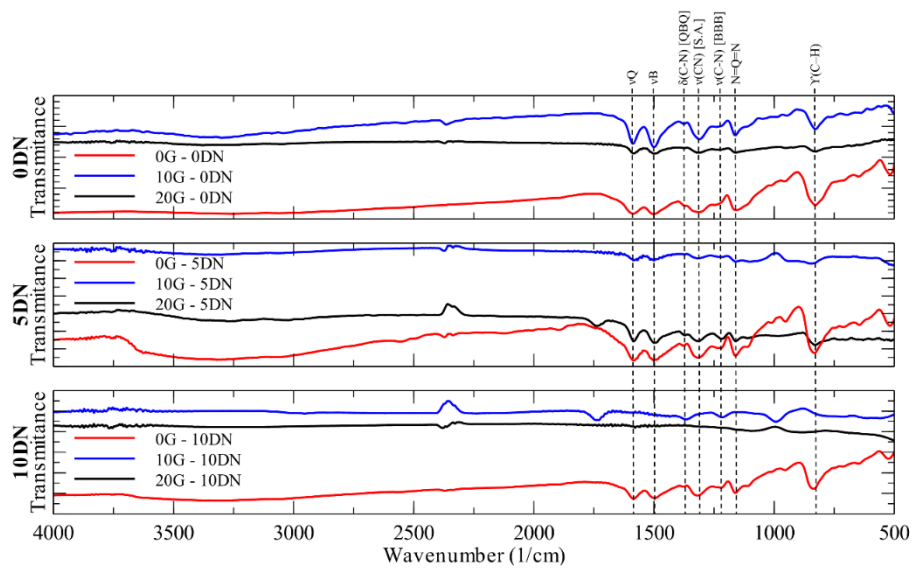
Figure 7 FTIR spectra of PANI/G/ND nanocomposites.

Figure 8 shows the SEM results for 0G – 0ND, 0G – 5ND, 20G – 0ND and 10G – 5ND samples. For the pristine PANI case, as shown in Figure 8a and Figure 8b, it is appreciated a granular structure characteristic of the precipitation polymerization process in strong acidic media (pH < 2.5) [52], [53]. For the 0G – 5ND sample, as shown in Figure 8c and Figure 8d, the resulting morphology is spherical with an average diameter close to 1μm. For the 20G – 0ND sample, as shown in Figure 8e and Figure 8f, the results show a laminar structure in a stacked arrangement. For both ND and G cases, the polymer seems to be coating the fillers, creating a core-shell morphology. The morphology for the 10G – 5ND case is a superposition of the G and ND case as shown in Figure 8g, Figure 8h and Figure 8i. Particularly, the ND-coated spheres deposit on G-coated nanosheets surfaces.
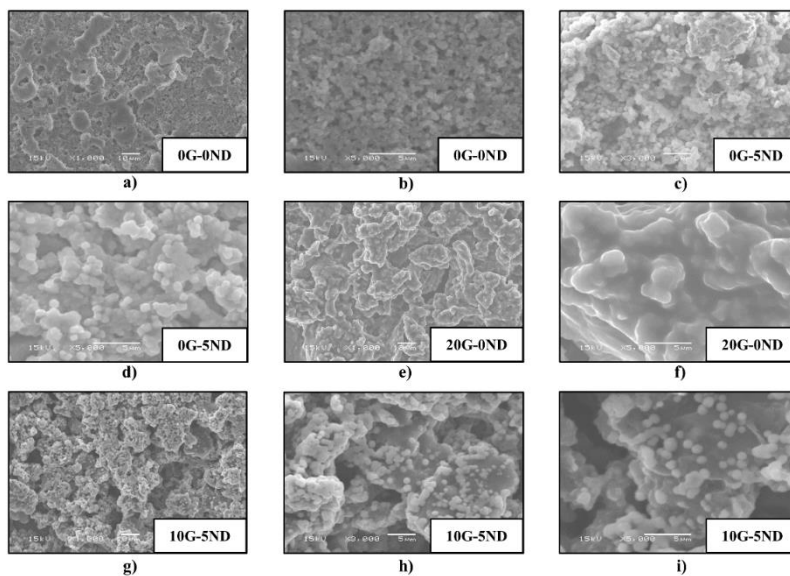
Figure 8 Representative SEM images of 0% G – 0% ND (a and b), 0% G – 5% ND (c and d), 20% G – 0% ND (e and f) and 10% G – 5% ND (g, h and i).

It is necessary to embed ND and G into the polymer matrix while avoiding agglomeration in order to truly form a nanocomposite. TEM results (Figure 9a) shows that lattice fringes are mostly between 2.5 nm - 5 nm length. The corresponding electron diffraction pattern (Figure 9b) shows three main bands assigned to the (1 1 1), (2 2 0) and (3 1 1) planes of diamond cubic crystal structure [54], [55]. Therefore, during composite synthesis large ND cluster formation is avoided by encapsulating the nanoparticles into polymer shells. Further, the results also suggests that the nanoparticles work as nucleation centers during polymerization.
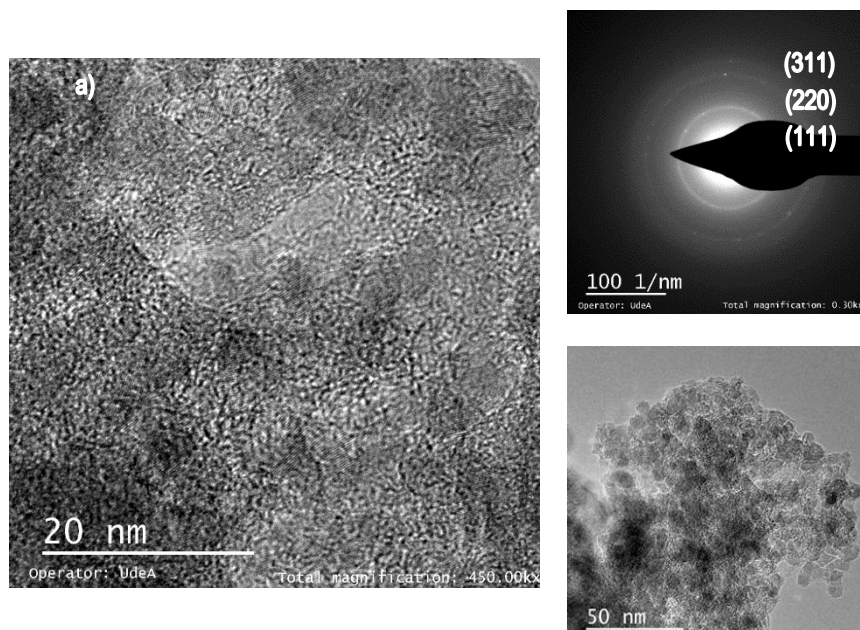
Figure 9 TEM images for 10% G – 10% ND Sample

TGA curves, as shown in Figure 10, reveal two mass loss stages: a first mass loss process around ~100°C attributed to the release of moisture and other volatile components, and a second process around ~490°C involving the degradation of PANI backbone [56], [57]. Changes on the thermal transitions of the polymeric phase due to filler loading were ascertained by performing DSC measurements. An endothermic process around ~100°C and an exothermic process around ~300°C were observed on DSC profiles for all the samples as shown in Figure 10. The endothermic process corresponds to the first mass loss stage recorded on TGA profiles (i.e. evaporation of volatile components). The exothermic process may be associated to a crystallization or crosslinking reaction considering that there is no significant mass loss recorded on TGA profiles during the corresponding temperature interval. Previous XRD studies on PANI (emeraldine base) reveals that from room temperature up to ~300°C there is no evidence of change in the degree of crystallinity of the polymer [56]. Therefore, the exothermic process around ~300°C involves a crosslinking

reaction and the proposed mechanism involves two adjacent –N=Q=N– groups that react to form two –NH=Q=NH– groups [57].
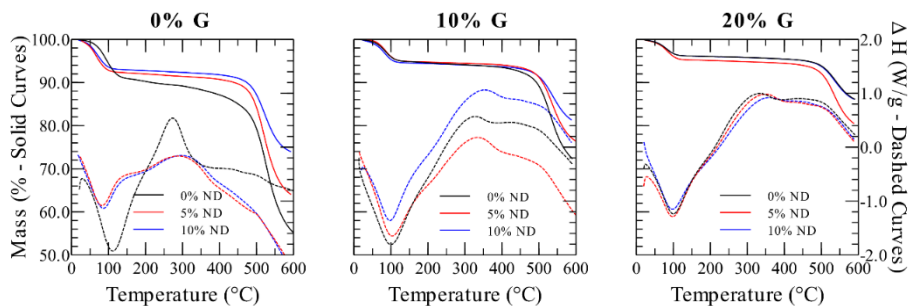


Figure 10 TGA and DSC results

Figure 11 shows the CV results for representative samples at 5mV/s. The CV profiles evidence two pair of peaks associated with leucoemeraldine ↔ emeraldine and emeraldine ↔ pernigraniline transitions [32]. The peaks indicate that the polymer retains its characteristic electroactivity despite the presence of the fillers. The peak currents showed a linear dependency with the square root of the scan rate (not shown) indicating that the diffusion of counter-ions within the film (in order to maintain the electroneutrality of the polymer) is the rate limiting process [58]. Furthermore, the shape of the voltammograms deviate significantly from a rectangular shape (characteristic of double-layer charging), indicating that the main charge storage mechanism involves the redox reactions of the bulk polymer.
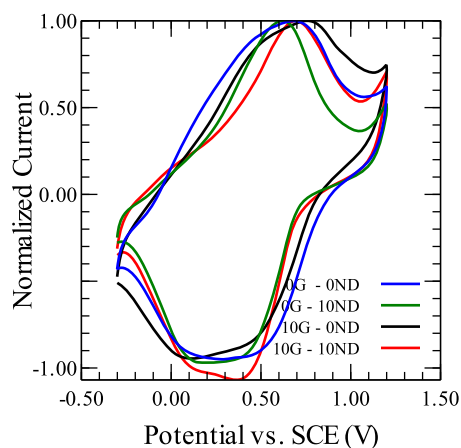
Figure 11 Cyclic Voltammetry results for representative samples at 5mV/s in 0.1M LiClO$_4$ in Acetonitrile.

From Figure 7 no significant peak shifts for PANI spectra can be appreciated due to the presence of different quantities of the additives. It is particular interesting to note that the strong peak close around ~829.4 cm$^{-1}$ is associated to the C–H out of plane bending vibrations of two adjacent hydrogen atoms on a 1,4 disubstituted benzene ring [49], [50], indicating a dominating *para*-coupling of polymer chains. Because *ortho*-coupling of chains may also occur, a dominating *para*-coupling indicates a low defect level in the conjugated structure [50]. The evidence of oxygen-containing functional groups in the 0G – 10ND and 10G – 10ND FTIR spectra could be attributed to the characteristic surface groups of detonation nanodiamond particles and can be present as a result of incomplete reduction of graphene from graphite oxide [51], [59].

The changes upon thermal cross-linking of composites in air at 150°C for 3 h are tracked using the improved sensitivity of Raman spectroscopy (Figure 12). The characteristics peaks at ~1160 cm$^{-1}$ and ~1220 cm$^{-1}$ are related to the C-H bending of the quinonoid and benzenoid rings, therefore, further confirming polymerization of polyaniline. The strong peak at ~1470 cm$^{-1}$ dominates the whole spectra and corresponds to the stretching of C=N bonds at quinonoid rings. The peaks at ~1330 cm$^{-1}$ and ~1380 cm$^{-1}$ correspond to the stretching vibrations of C-N$^{+\bullet}$ bonds, suggesting incomplete

29

deprotonation. The band at ~1405 cm$^{-1}$ is associated to substituted phenazine segments indicating branching (cross-linking) of polymer chains.
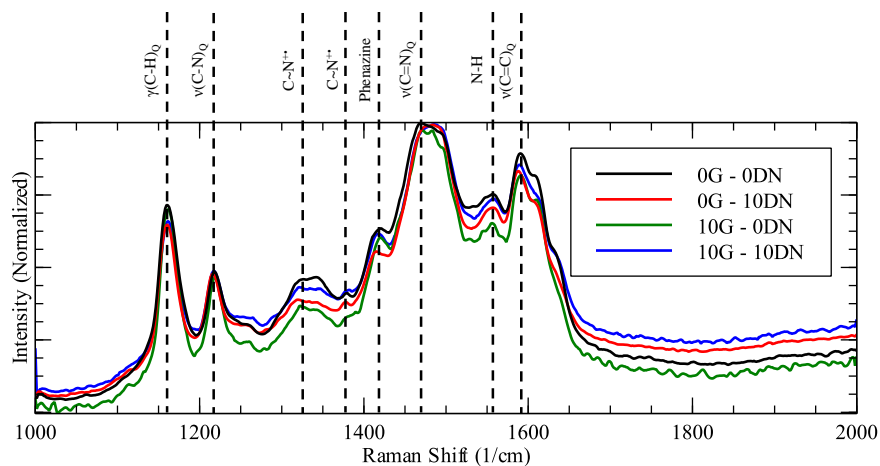


Figure 12 Raman spectra for selected compositions upon thermal cross-linking

The core-shell morphology shown by the SEM and TEM results suggest a particular interaction during the polymerization reaction between monomer and fillers. As there is no evidence of new bonds or significant peak shifts in the FTIR results, the nature of the interaction between the polymer and the nanostructures might involve only orbital distortion and/or charge redistribution. Under strong acidic media, aniline molecules transform into anilinium cations [52], [53]. When the nanostructures are added to the reaction mixture, anilinium cations may be attracted towards the surface of G and ND by electrostatic interactions, as shown in Figure 13. The π-conjugated structure of G and the functional groups on the surface of ND play a special role in this regard. Therefore, the polymerization reaction could start at the surface of the fillers once the oxidizing agent is added to the mixture [52]. Furthermore, the π-conjugated structure of G may interact with the conjugated structure of already formed polyaniline by π-stacking. Consequently, it is suggested that the polymer chains grows adhered to the surface of the fillers explaining the formation of core-shell morphology. The core-shell structure evidenced further explain the decrease in the intensity of PANI peaks in the FTIR results as the nanostructure content

increases: the constrained motion of the chains implies a restriction on the intensity for different modes of vibration. Depending on the ratio between aniline and nanostructures, there may be cases where the nanostructure is not wrapping or partially wrapping the polymer as shown in Figure 14. The presence of "excess" or partially wrapped G nano-sheets explains the appearance of peaks associated to functional groups on the surface of the nanostructure as well as featureless spectra (e.g. 20G – 10ND case) similar to the spectrum of pristine graphene.
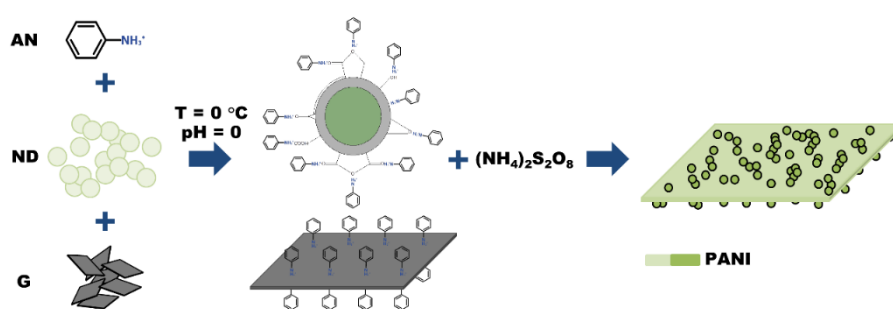


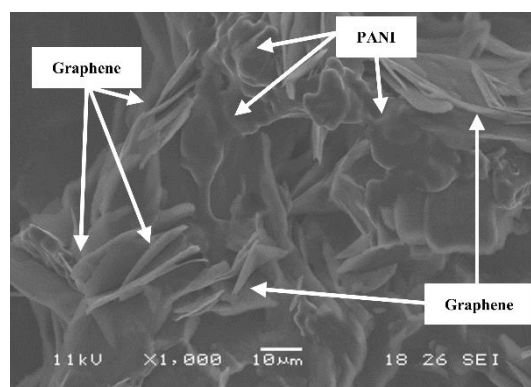Figure 13 Schematic of the formation of core-shell morphology.



Figure 14 SEM image of 20% G – 0% ND Sample showing excess graphene partly covered by PANI.

As seen in Figure 8i, polymer-coated ND particles deposit on G surface, thus preventing the major re-stacking of the nanosheets. A comparison of the ratio between electroactive area (by chronoamperometry measurements) and geometrical area reveals that for the 10G – 5ND case the ratio is ~3.3 compared to ~2.0 for 10G – 0ND sample and ~1.8 for the 0G – 5ND sample. Therefore, it is clearly seen than the synergy between G and ND is

beneficial for energy storage as the accessibility and the transport kinetics of ions across the electrode increases, thus leading to more polymeric material to participate during redox transformations.

The thermal stability of the nanocomposites is positively affected by the filler content as evidenced in Figure 10. For PANI, the mass lost during the first stage (~100°C) is as much as ~10%, which may also indicate the outgassing of unknown molecules and/or incomplete de-protonation [56]. For the nanocomposite cases, the mass lost during the first stage decreases as the filler content increases. As stated before, the second mass lost process (~300°C) is associated to the degradation of the polymeric phase. The temperature of decomposition (Onset) and the mass lost at 600°C for such process is compared in Figure 15a for all the samples. The mass lost at 600°C is reduced to 13% for the 20G – 10ND case compared to 48% for pristine PANI. The temperature of decomposition is delayed as much as ~13°C for the 10G – 5ND case compared to bare PANI. The graph reveals that G has a more marked effect compared to ND, and there seems to be insignificant interaction between the fillers due to the parallelism of the curves. Based on the aforementioned behavior, the interaction term was used as an unbiased estimate of the error in order to perform a statistical analysis of the experiment [60]. An ANOVA test (Appendix Table 6) concludes that both G and ND have a statistical significant effect on the temperature of decomposition. Furthermore, a Fisher's Least Significant Difference (LSD) test concludes that 10% G and 20% G loads gives statistically equal results. The main mechanism for thermal enhancement by layered fillers like G is due to a barrier effect: a slow down on the diffusion of degradation products from the polymer phase to the gas phase [61]–[63]. Strong $\pi$-$\pi$ interactions between polymer and filler conjugated systems may also play a significant role in this regard. Therefore, the behavior of the Temperature of Decomposition with G load from 10% to 20% is due to an excess of G in the reaction mixture (Figure 14). The thermal enhancement, either by a barrier effect or Van der Waals interactions, is marginal

for partially wrapped G. On the other hand, the LSD Test performed on the Temperature of Decomposition concludes that 0% ND and 10% ND loads give statistically equal results. The mechanism of thermal enhancement by ND is explained in terms of nano-confinement: the chain mobility around the filler is restricted resulting in changes in the dynamics of the thermal transition processes [64]. As the ND concentration rises, so does the probability of the filler to form large aggregates. Therefore, the interfacial area between the filler and the matrix decreases. The nanocomposite effect is lost, and the material starts to behave as a microcomposite if the filler continues rising.
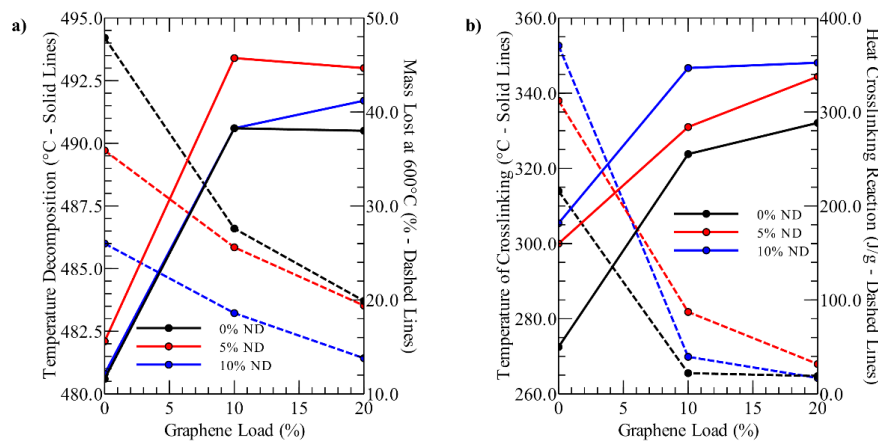


Figure 15 a) Temperature of Decomposition and Mass Lost at 600°C, b) Temperature of Crosslinking and Heat of Crosslinking Reaction.

The addition of different quantities of nanostructures has a marked effect on the peak temperature for crosslinking as well as the heat released during such process as shown in Figure 15b. The tendency observed reveals that, as the nanostructure load rises, an increase in the peak temperature for crosslinking is observed. Such increase in the peak temperature might indicate that the activation energy required for the starting of the crosslinking reaction rises. The corresponding ANOVA (Appendix Table 7) test concludes that both G and ND have a statistical significant effect on the peak temperature of crosslinking. Furthermore, a LSD test confirms that the peak temperature increases monotonically with the increase in filler content. The increase in the activation energy might be explained by some interaction

33

between the fillers and the polymer nitrogen atoms. Particularly, for PANI/G nanocomposites, it has been proposed the formation of charge-transfer dipolar attractions [65]. It is particularly interesting to notice that, for the PANI/ND composites, the heat released during the course of the crosslinking reaction increases with ND content. This behavior is consistent with the assumption of interactions at polymer/nanostructure interfacial area because the amount of energy released is related to the difference between the energy state of the bonds formed during crosslinking and the previous bonds suggested between the polymer and filler. On the other hand, it is noted that by the addition of G the energy released diminishes. This behavior may be explained by the formation of barriers between adjacent chains due to the filler. Therefore, not all the chains have the opportunity to crosslink because there is a physical restriction and the released energy diminishes with filler load.

The composites are electrochemically evaluated and screened performing an accelerated cycle life test consisting on exposing the samples to 100 charge/discharge cycles at 1 A/g and a potential window of 3000 mV in a two electrode set-up (working electrode vs. carbon rod). The accelerated cycle life test is intended to simultaneously asses the electrode performance under cyclic volume change and high anodic potentials. Polyaniline is known to degrade at potentials larger than 0.7 V vs. Ag/Ag$^+$ in organic solvents [66]. The mechanism of degradation is believed to be associated with chain breaking as no major change in the structure of the polymer has been evidenced. However, in the absence of a source of protons, such as in a blank aprotic electrolyte, decomposition seems to be associated with a decrease of proton content leading to electro-inactivity [67].
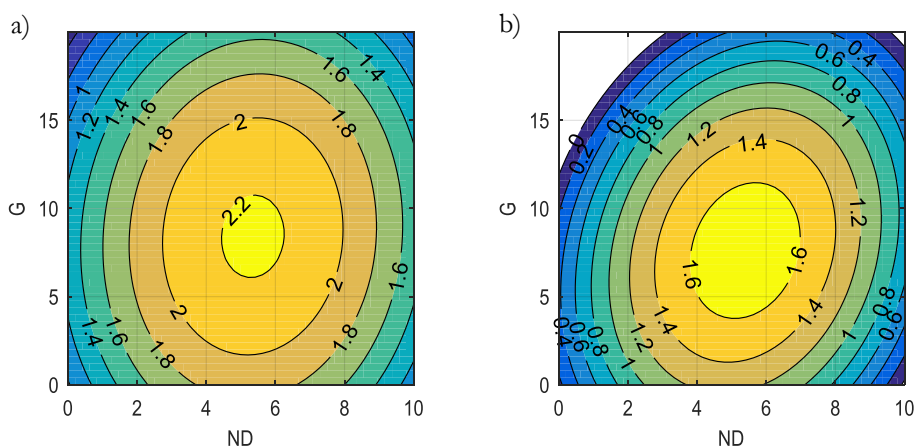
Figure 16 Initial (a) and final (b) relative capacitances of PANI/ND/G composites. The capacitances are normalized with respect to the initial capacitance of pristine PANI sample.

Figure 16 shows contour plots of the capacitance of the composites as a function of ND and G compositions. The plots were generated by fitting a quadratic polynomial regression model. For both cases, the capacitances are measured relative to the capacitance of an un-cycled pristine PANI sample. Case a) represents the initial capacitance of the samples prior to cycling. Case b) represents the final capacitance of the samples after exposed to the accelerated charge/discharge test previously described. The results suggest that the maximum capacitance and capacitance retention is reached for a composition around 5 wt. % ND/AN and 10 wt. % G/AN. The initial gravimetric capacitance for this sample is ~120 F/g at 1 A/g. The results indicate that excess G or ND do not improve charge storage performance of the polymer because of partial coverage of the fillers as previously evidenced from microscopical observations (Figure 14). Also, the interaction between G and ND is critical, presumably due to the spacer role of ND for G sheets.

# 5 Polyaniline Core-Shell Structures with Cellulose-Nanocrystals†

## 5.1 Background

Results from Chapter 4 indicated the possibility of forming polyaniline core-shell composites by in-situ polymerization of cationic aniline in presence of negatively charged templates. In this regard, nano-crystalline cellulose is identified as a template for the formation of a more open electrode structure to help boost charge transfer and transport electrode thickness of polyaniline electrodes. Sulfuric acid hydrolysis of cellulose fibers results in colloidal suspensions of Cellulose Nanocrystals (Cellulose I) electrostatically stabilized by deprotonated anionic $-OSO_3$ groups grafted at the sites of hydroxyl groups as a consequence of the nature of the process. According to Lu and Hsieh [68], the mechanism for acid hydrolysis of cellulose involves protonation of either glucosidic or cyclic oxygen. Protonation is followed by chain-scission as break-down of glucosidic bonds is induced by bonding with water. Amorphous regions will react first implying that the reaction could be stopped to leave behind the crystalline regions intact. Esterification of hydroxyl groups occurs in parallel to acid hydrolysis leading to the presence of sulfate groups on nano-crystal surface.

## 5.2 Experimental Procedure

In situ formed films were prepared by immersion of graphite rod electrodes in the reaction media. Graphite rod electrodes were previously electrochemically cleaned in 1M $H_2SO_4$. The reaction media consisted of a mixture of aniline (AN), ammonium persulfate (APS) and a nano-crystalline cellulose (CNC) suspension, diluted in 1M $H_2SO_4$. Nano-

---

† Disclaimer: Contents of this chapter have been published in the ASME 2017 International Mechanical Engineering Congress and Exposition official proceedings.

crystalline cellulose suspension were prepared through acid hydrolysis of cotton linters as reported by Ivanova and coworkers [69] (refer to Figure 17). The polymerization reaction were performed at low temperature (0°C - 5°C) for 24 hours. The graphite electrodes were subsequently rinsed in deionized water and dried at 80°C for 24 hours prior to electrochemical characterization. Ten samples were prepared according to a D-Optimal Mixture Design on the variables AN, APS and CNC (refer to Figure 18).
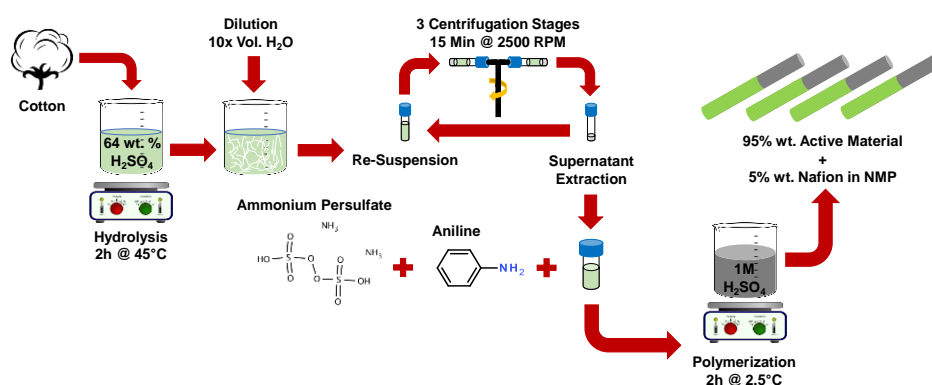


Figure 17 CNC extraction and aniline polymerization protocol

Electrochemical characterization was performed on a three electrode cell consisting of the corresponding graphite electrode as working electrode, Ag/AgCl as reference electrode, platinum as counter electrode and 1M $H_2SO_4$ as the electrolyte. Cyclic voltammetry were performed at a potential window of (-200 mV, 800 mV) and at different scan rates (5 mV/s to 100 mV/s). Electrochemical Impedance Spectroscopy (EIS) were recorded at the Open-Circuit Potential (OCP) of the corresponding modified electrode. The frequency varied among 100 kH – 100 mH and the voltage amplitude was 5 mV.
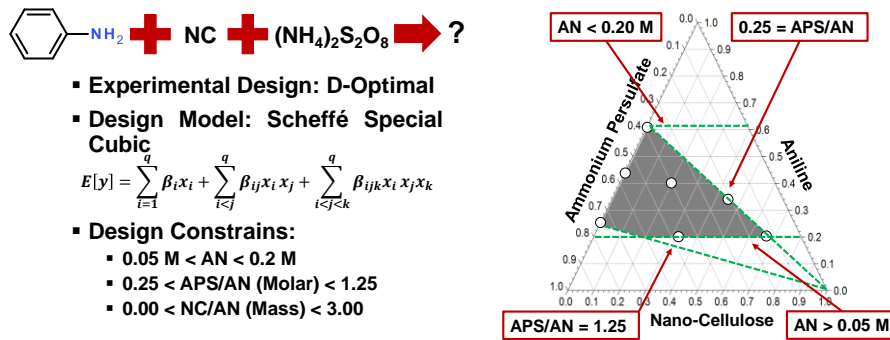
- **Experimental Design: D-Optimal**
- **Design Model: Scheffé Special Cubic**

$$E[y] = \sum_{i=1}^{q} \beta_i x_i + \sum_{i<j}^{q} \beta_{ij} x_i x_j + \sum_{i<j<k}^{q} \beta_{ijk} x_i x_j x_k$$

- **Design Constrains:**
  - **0.05 M < AN < 0.2 M**
  - **0.25 < APS/AN (Molar) < 1.25**
  - **0.00 < NC/AN (Mass) < 3.00**

AN < 0.20 M | 0.25 = APS/AN
APS/AN = 1.25 | Nano-Cellulose | AN > 0.05 M

Figure 18 Experimental design for CNC/PANI synthesis

## 5.3 Material Characterization and Analysis

Cyclic voltammetry measurements were performed in order to gather the electrochemical fingerprint of the films. The curves for representative samples is presented in Figure 19. For all the cases, it is evidenced a broad and sharp peak in the anodic region followed by a current plateau as the potential increases until the scan is reversed. The sharp peak is associated to the polyaniline redox conversion from Leucoemeraldine (L) to Emeraldine (E) state [36]. The current plateau is a consequence of a double-layer charging phenomena. It is more noticeable after the peak as the conductivity of the E state is higher than that of the L state. The cathodic region resembles the aforementioned phenomena reversed. The characteristic hysteresis of CEP films is evidenced by the clear difference between anodic and cathodic peak potentials.
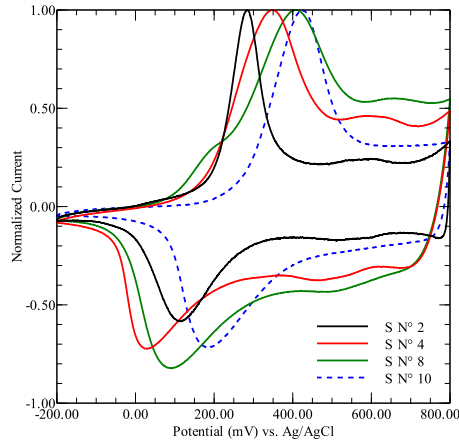
Figure 19 Cyclic voltammetry data for selected samples recorded at 50 mV/s in 1M $H_2SO_4$.

The dependency of peak current with scan rate allows a practical identification of the dominating charge storage mechanism. The peak current and scan rate relationship could be expressed by a power law as [70]:

$$i_P = av^b \qquad (1)$$

Where $v$ represent the scan rate, $a$ and $b$ regression coefficients, and $i_P$ the peak current. Two extreme cases could be defined. First, for $b = 1.0$ the peak current is directly proportional to the scan rate indicating double-layer charging mechanism. On the other hand, for $b = 0.5$ the peak current is proportional to the square root of the scan rate, indicating a diffusion controlled mechanism characteristic of faradic processes. The b-values for the tested samples are presented in

Table 3. The data suggest a mixed charge storage mechanism for the cathodic and anodic region which seems to vary among samples. It is worth noting that, the b-values for the cathodic scan are closer to 1.0 consistent with the double-layer charging current preceding the peak. In either case, an Analysis of Variance is performed concluding that there is not significant statistical difference for the b-values among the tested samples. This

suggests that the charge storage mechanism is in essence the same for the explored experimental region.

Table 3 Mass proportion of each sample and corresponding b-value for anodic and cathodic peaks.

| Sample | Mass Proportion | | | b-value | |
|--------|-----|------|------|--------|----------|
|        | AN  | APS  | CNC  | Anodic | Cathodic |
| 1  | 0.20 | 0.47 | 0.33 | 0.86 | 0.95 |
| 2  | 0.39 | 0.41 | 0.20 | 0.83 | 0.95 |
| 3  | 0.62 | 0.38 | 0.00 | 0.83 | 0.98 |
| 4  | 0.62 | 0.38 | 0.00 | 0.71 | 0.86 |
| 5  | 0.25 | 0.75 | 0.00 | 0.76 | 0.85 |
| 6  | 0.20 | 0.47 | 0.33 | 0.77 | 0.89 |
| 7  | 0.44 | 0.56 | 0.00 | 0.78 | 0.91 |
| 8  | 0.25 | 0.75 | 0.00 | 0.84 | 0.94 |
| 9  | 0.36 | 0.22 | 0.43 | 0.83 | 0.89 |
| 10 | 0.20 | 0.12 | 0.68 | 0.92 | 0.93 |

The gravimetric capacitance of the films were calculated from voltammetry data according to [71]:

$$C_m = \frac{\int_{t(V_i)}^{t(V_f)} I(t)dt}{m(V_f - V_i)} \tag{2}$$

Where $I$ represent the instantaneous cathodic current, $t$ the time, $V_i$ the initial potential of the cathodic scan, $V_f$ the final potential of the cathodic scan and $m$ the mass of the film. The data of the films gravimetric capacitance calculated according to the previous equation (at 5 mV/s) is presented in the ternary plot shown in Figure 20. The data adjusts to a Scheffé special cubic polynomial model across the experimental region.
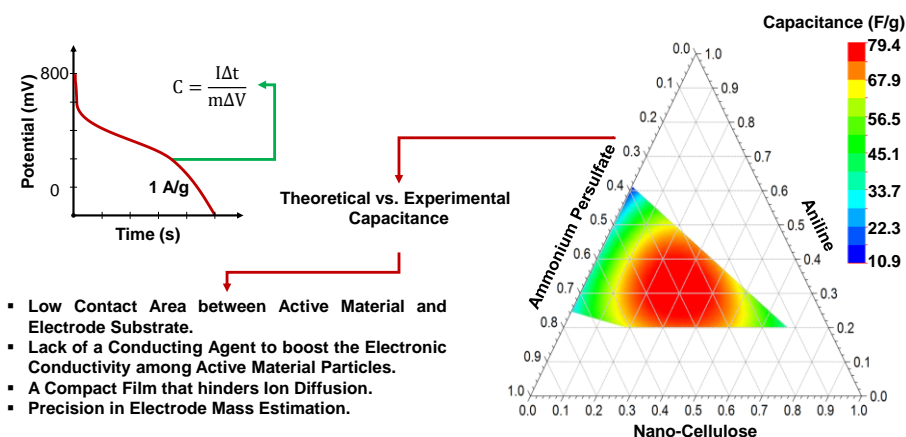
Figure 20 Ternary plot diagram for the capacitance adjusted to a Scheffé special cubic polynomial model.

The data suggest that the maximum reported capacitance of the films, within the experimental region, is achieved by the inclusion of the nano-crystalline cellulose suspension during the polymerization reaction. The previous conclusion is a consequence of the predicted capacitance values along the side of the triangle connecting vertex AN to vertex APS, that is, for those cases were CNC proportion is zero. However, the capacitance of the films does not increase monotonically as the CNC mass proportion does. Otherwise, the maximum attainable capacitance region would be located near the CNC vertex. The role of CNC on the mixture could be explained as a template effect as a previous conclusion indicated that the charge storage mechanism remain the same among samples. The template effect is associated with the formation of a more open structure for the polymer as it coats the surface of CNC whiskers. Therefore, increasing the surface area accessible for the electrolyte and enhancing the charge transfer reaction within the bulk of the polymer. In other words, more polymer is capable of experimenting the corresponding redox transformation within the time scale of the experiment, then boosting the charge stored. Excess CNC on the mix would be detrimental as partially coated or uncoated whiskers could hinder electronic conductivity of the films. Through Raman analysis it is confirmed the presence of PANI polymer for all the samples (refer to Figure 37)

A theoretical capacitance for the film material ($C_T$) could be estimated assuming that the polymer is the only material experimenting redox transformations and neglecting the double-layer charging contribution:

$$C_T = \frac{\alpha F}{M \Delta V} \qquad (3)$$

In the previous equation, $\alpha$ is the electron-per-monomer ratio for the corresponding redox transformation, $F$ the Faraday constant (96 458 C/mol), $M$ the molecular mass of the polymer (91 g/mol) and $\Delta V$ the potential window within transformation occurs.

The cyclic voltammetry data suggest $\alpha = 0.5$ as only the L↔E transformation appears active within the 1000 mV potential window. Therefore the estimated theoretical capacitance is 530.1 F/g. The reported capacitance values are one order of magnitude below the theoretical calculation. The aforementioned could be explained by several factors such as (but not limited to):

- Extension of contact area between active material and the electrode substrate. Contact area could be improved by applying pressure on the electrode.
- Lack of a conducting agent to boost the electronic conductivity among active material clusters.
- A compact film that hinders ion diffusion.
- Precision in electrode mass estimation.

The selection of the proper electrode mass for capacitance calculation is perhaps the most influential factor accounting the difference between reported data and theoretical predictions. The electrode masses were measured by direct weighting implying that the mass measured is the addition of (but not limited to) the mass of the polymer, the mass of the nano-crystalline cellulose, the mass of the hydrogen sulfate ions doping the polymer and possibly some moisture retained. If we consider the sulfate ions mass, the previous theoretical calculation drops to 345.8 F/g. Further, for those cases were CNC was added, if we consider (as an illustrative example) that the polyaniline proportion on the deposited

42

films ranges between $0.20 - 0.40$ then the capacitance theoretical prediction drops even further to $69.1$ F/g $- 138.3$ F/g.

Figure 21 shows the Nyquist plots for Sample 4 and Sample 9 before and after 1000 load/discharge cycles. The samples differentiate on the absence/presence of CNC on the mixture as the relative proportion APS-to-AN remained constant at 0.6. The impedance spectra of an electrochemical capacitor material, such as activated carbon, is widely described according to a transmission line equivalent circuit. The corresponding Nyquist plot will contain to main sections: a 45° segment and an almost vertical line at the low frequency region. Therefore, the addition of CNC further improves a capacitive-like behavior for the polymer as evidenced by comparing the spectra of Sample N° 9 versus Sample N° 4. Further, it is noted that the Electrochemical Series Resistance for Sample N° 4 remains almost constant while that for Sample N° 9 diminishes after cycling. The length of the 45° section is correlated with the resistance of the ion flow across the film. The almost null 45° section at the Sample N° 9 supports the theory of enhanced surface area by the templating effect of CNC. Further, upon cycling, the voltammetric peaks seem to be more spread and less sharp indicating a possible collapse of the porous structure (refer to Figure 22).
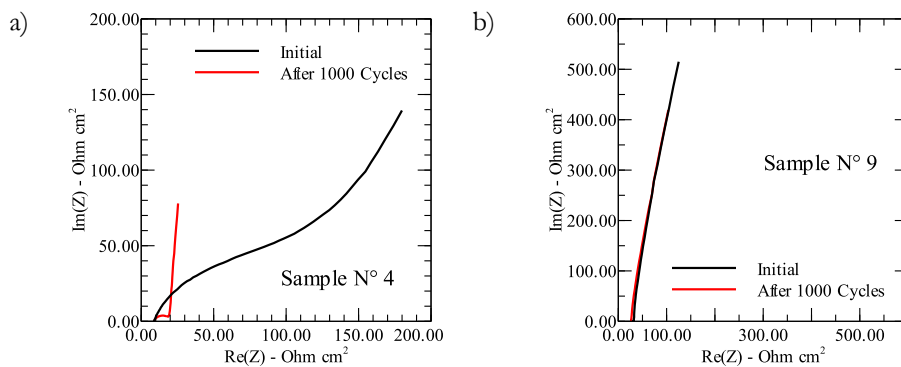


Figure 21 Nyquist plot for Sample N° 4 (a) and Sample N° 9 (b) before and after 1000 charge/discharge cycles.

Cycling stability can be further evaluated from EIS data according to [71]:

$$C_{EIS} = \frac{1}{2\pi f Im(Z)} \qquad (4)$$

Where $f$ represent the frequency and $Im(Z)$ the imaginary component of the spectra at that particular frequency. The chosen frequency is often that at which the phase angle is -45°. A capacitance retention could be evaluated by comparing the capacitance of the corresponding sample before and after cycling according to equation (4). The capacitance retention ability is evaluated for Sample N° 4 and Sample N° 10 in Figure 21. For the aforementioned samples, the relative proportion APS-to-AN remains constant at 0.6 but the latter has a higher CNC load than the former. The capacitance retention for sample N° 9 is 123.7% while that for Sample N° 10 is 118.2%. The increased capacitance after cycling couples with the concomitant decrease on ESR as previously mentioned.
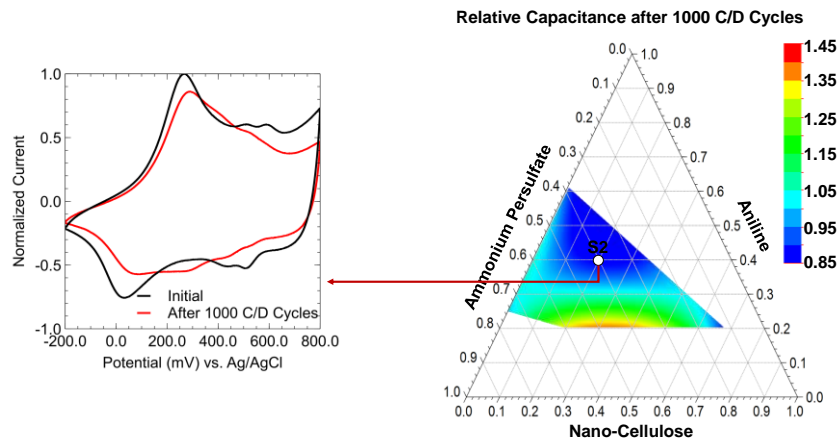


Figure 22 Capacitance retention upon cycling of PANI/CNC electrodes

# 6 Few-Layer Aqueous Graphene Dispersions by Cellulose Nanocrystals‡

## 6.1 Background

Reduction of graphene oxide (GO) is recognized as a viable route towards mass production of graphene (G) [72]. However, the poor colloidal stability of reduced graphene oxide (rGO) in common solvents represents a difficulty for further processing [73]. Stable aqueous rGO dispersions (without the need for either polymeric or surfactant stabilizers) are possible by electrostatic repulsion of remaining oxygen-containing functional groups after its reduction from graphene oxide [74]. That is, as a result of incomplete reduction of graphite oxide. Incomplete reduction leads to a higher deviation of the properties of rGO compared to the mechanically cleaved or pristine G (defect-free carbon monolayer).

On the other hand, dispersions of low- to zero-defect G have been achieved upon direct exfoliation of graphite [75]. Exfoliation is most effectively performed by sonication as the main energy source to break apart graphite into individual G sheets. Although more than 50 solvents have been tried, organic solvents like N-Methyl-2-pyrrolidone, Dimethyl Sulfoxide, and Dimethylformamide have shown to be the most effective in this regard. Water is a desirable solvent from a manufacturing perspective due to its availability and minimal health and physical hazards associated with its handling and storage compared to the aforementioned solvents. However, the lack of oxygen-containing functional groups in low- to zero-defect G leads to sheet agglomeration or restacking in water. Therefore, dispersion of low- to zero-defect G benefits from the use of a stabilizer.

From Chapter 4 it was evidenced the spacer role of diamond nanoparticles to prevent large graphene (G) sheet agglomerates formation. Therefore, reduction of GO is performed

---

‡ Disclaimer: Contents of this chapter have been published in the ASME 2018 International Mechanical Engineering Congress and Exposition official proceedings.

in the presence of a stabilizer to evaluate its suitability for promoting low- to zero-defect rGO dispersions in water. Cellulose Nanocrystals (CNC) highlight as an abundant and environmentally friendly option in this regard. Further, CNC could be used as a template and mechanical property enhancer towards the construction of freestanding flexible conducting films or the formation of foams/aerogels for electrochemical energy storage.

GO is preferred as the starting material versus directly exfoliated graphite by sonication because of the scalability issues that hinder its cost-effectiveness for large-scale processing. GO is obtained by electrochemical oxidation of graphite because it has proven to produce GO with a lower defect content compared to the traditional Hummers and Offeman method [76]. rGO is produced by subcritical water reduction of GO as a more sustainable alternative compared to hydrazine reduction [77].

## 6.2  Experimental Procedure

GO were exfoliated by electrochemical oxidation of graphite based on the two-step approach reported by Cao and coworkers [76]. The set-up consisted of two graphite rods (d = 10 mm) separated by 45 mm (center to center). First, a voltage of 2.2 V was applied and held constant (without current limiting) for 5 minutes in 30 ml of 95 wt. percentage $H_2SO_4$. Then, the voltage is raised to 10 V and held constant for 55 min while the electrodes were immersed in 30 ml of 0.1 M $Na_2SO_4$. After the exfoliation process, the suspension is placed in an ion-exchange membrane and dialyzed against de-ionized water until the conductivity remained constant. The suspension is sonicated for 30 minutes and then centrifuged (Centrific Model 228) for 1h. The supernatant is collected and stored for further use. CNC suspension was prepared through sulfuric acid hydrolysis of cotton linters as reported in a previous author's communication [78].

CNC/GO aqueous dispersions were prepared by varying the mass proportion of CNC relative to GO (0 - 20) and bath sonicated for 30 mins. The samples are identified as xx:1

CNC/GO where xx stands for the mass proportion of CNC relative to GO. A Teflon-Lined autoclave was used during the hydrothermal treatment (HT) of GO/CNC dispersions. HT was performed at 150 °C and 180 °C for 1-10 hours. Refer to for a schematic description of the synthesis protocol.
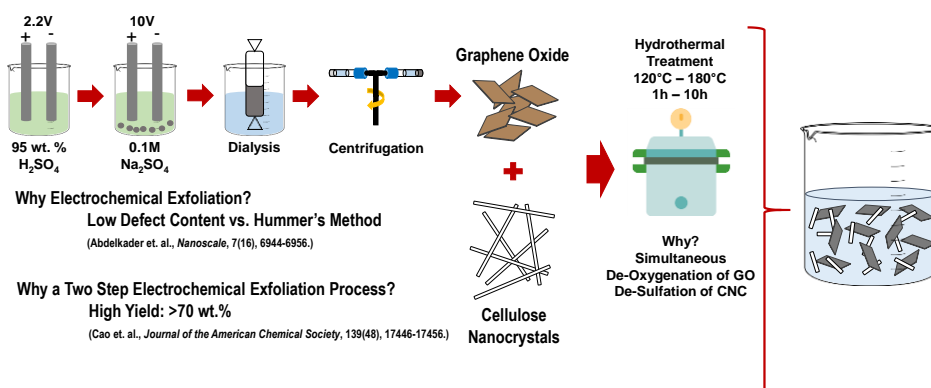


Figure 23 Synthesis protocol for G/CNC aqueous dispersions

## 6.3 Dispersion Characterization and Analysis

GO has been traditionally obtained by modifications of the Hummers and Offeman method. One downside of the mentioned process is the hazardous and corrosive characteristics of the reactants and products mainly involved besides graphite and water: $NaNO_3$, $KMnO_4$ and concentrated $H_2SO_4$. In this regard, electrochemical exfoliation offers an attractive approach because oxidation is achieved by the reaction between graphite (as an anode) and nucleophilic water molecules (present in the electrolyte). Further, less disruption of the G conjugated structure has been attained by this method. Following the two-step approach reported by Cao and coworkers [76], graphite rods are first charged in concentrated sulfuric acid to promote the formation of a graphite intercalation compound by the insertion of ions between the graphite sheets. Oxidation and exfoliation are then performed in a 0.1 M $Na_2SO_4$ solution. IR spectrum for electrochemically exfoliated GO (refer to GO in Figure 24) suggests the presence of a broadband around 3400 cm$^{-1}$ (O–H) and three peaks at 1578 cm$^{-1}$, 1400 cm$^{-1}$ and 1100 cm$^{-1}$ attributable to C=C (aromatic ring),

C–OH (alcohol) and C–O (epoxy), respectively [79]. C–OH group vibrations could be overlapped within the peak at 1100 cm$^{-1}$. The IR spectra confirm the low-defect quality of GO sheets obtained by electrochemical exfoliation.
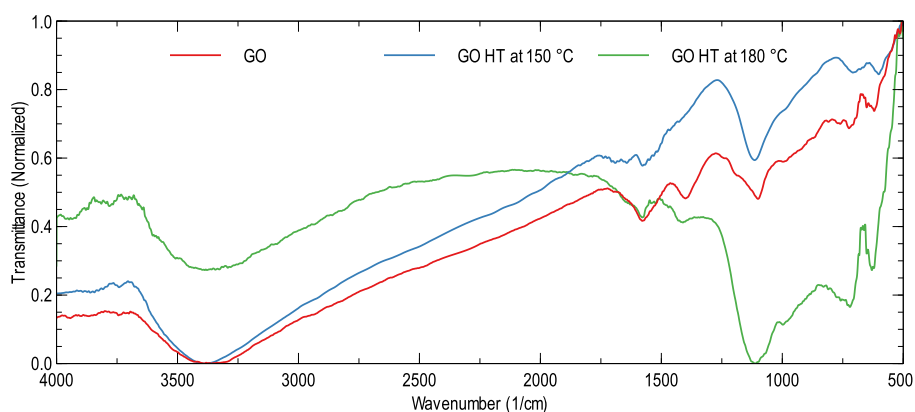


Figure 24 IR Spectra of GO

CNC is obtained by sulfuric acid hydrolysis of cotton linters. There IR spectra of CNC (refer to CNC in Figure 25) reveals four main regions: O-H groups involved in hydrogen bonding (3000 – 3600 cm$^{-1}$), C-H (2800 – 2900 cm$^{-1}$), C-O (1050 – 1100 cm$^{-1}$) and rocking vibration of C-H groups (700 – 720 cm$^{-1}$) [80]. The strong peak around 1637 cm$^{-1}$ is associated with adsorbed water [81]. The presence of notorious peaks at 1428 cm$^{-1}$ (CH$_2$ scissoring) and 897 cm$^{-1}$ (β-glycosidic linkages) suggests the predominance of Cellulose I crystal structure [82]. CNC extracted by sulfuric acid hydrolysis bears sulfate half-ester functional groups on its surface. Colloidal suspensions of CNC in water are formed by electrostatic repulsion of fibrils due to de-protonated sulfate half-ester functional groups. The evidence of sulfate half-ester functional groups attached to CNC could be seen by the presence of peaks at 1030 cm$^{-1}$, 1160 cm$^{-1}$ and 1370 cm$^{-1}$ associated to S=O vibrations [83], [84]. Further, the peak at 807 cm$^{-1}$ is associated with the symmetrical C–O–S vibration of the C–O–SO$_3$ group [85], [86].
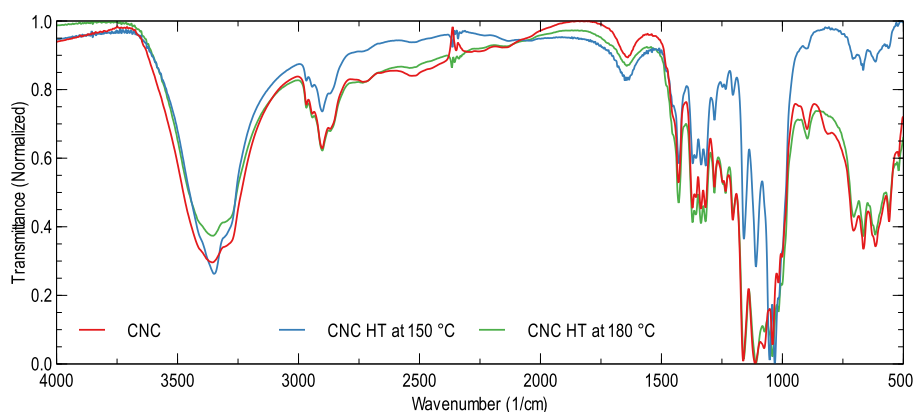
Figure 25 IR Spectra of CNC

The formation of stable G dispersion in water has shown to depend strongly on the nature of the surface charge of the stabilizer agent. Cationic stabilizers are ascribed to have a lower graphene exfoliation efficiency because of the affinity of cations to bind with $\pi-$ conjugated systems leading to a reduction in the electrostatic repulsion among sheets [87]. In this regard, an aqueous colloidal suspension of CNC is a favorable environment for this purpose due to the negative charge associated with de-protonated sulfate half-ester functional groups. Therefore, the reduction of an aqueous GO dispersion in the presence of CNC should promote the formation of stable rGO dispersions. The advantage of starting with GO, instead of graphite exfoliation in CNC suspension, is the elimination of extensive sonication to exfoliate the sheets. Reduction of GO is further performed following a hydrothermal approach. Here it is understood as hydrothermal treatment as those processes carried on using subcritical water as a reaction media. Specifically, within temperature and pressure ranges of 150 °C < T < 370 °C and 0.5 MPa < P < 22 MPa. CNC/GO aqueous dispersions are prepared, loaded in an autoclave and treated at 150 °C or 180 °C for 10 hours. For all the cases, the concentration of GO relative to water is maintained at 0.1 mg/ml to eliminate the possibility of irreversible cross-linking reactions between sheets.
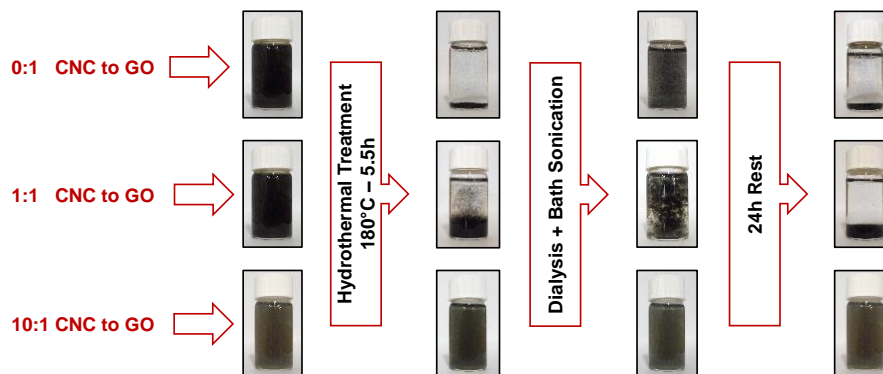
Figure 26 Selected GO and CNC/GO dispersions before and after HT at 180 °C for 5.5 hours

Figure 26 shows the physical appearance of GO dispersions prior and after HT at 180 °C for 5.5 hours. Upon HT, it is noted that the colloidal stability of GO seems to be compromised due to the presence of macroscopic clusters. However, for the case of 20:1 CNC/GO a stable dispersion preserve after treatment. These dispersions are further characterized by UV-Visible spectroscopy. The UV-Visible spectrum of GO produced by the Hummers and Offeman method shows a peak at 230nm ($\pi$-$\pi$* transition of aromatic C-C bonds) and a shoulder at 300nm ($\pi\rightarrow\pi$* transitions of C=O bonds) [88]. However, the UV-Visible spectrum of electrochemically exfoliated GO is dominated by a marked adsorption peak around 255 nm (refer to GO in Figure 27). This peak could be associated with a bathochromic shift of the $\pi$-$\pi$* transition of aromatic C-C bonds due to increased conjugation. The lonely peak depicted in the UV-Visible spectra is in agreement with the functional groups on GO detected by IR spectroscopy. After HT, a reduction in absorbance is appreciated. This reduction is associated with the evident agglomeration shown in Figure 26.
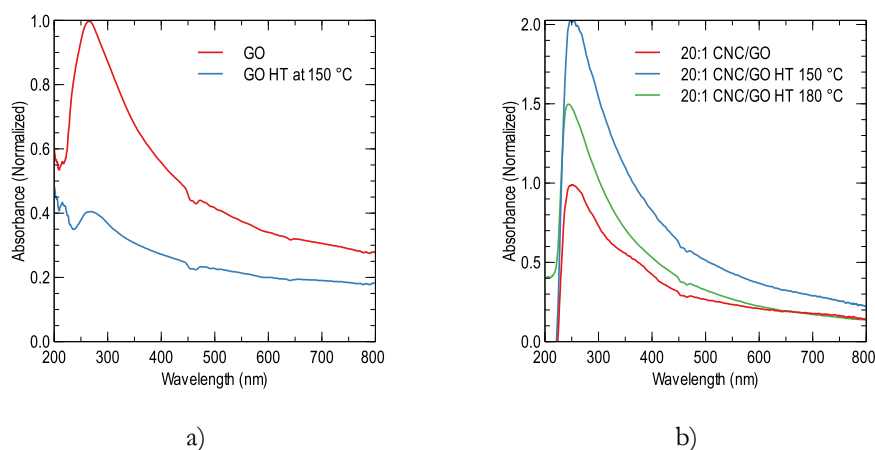
Figure 27 UV-Visible spectra for 0:1 and 20:1 CNC/GO before and after HT. These curves are normalized in each case relative to the absorbance profile of untreated dispersions

IR spectra are analyzed in order to see the effect of HT on the evolution of oxygen-containing functional groups on GO. After HT at 150 °C for 10 hours (refer to GO HT at 150 °C Figure 24), the main difference is the disappearance of the peak at 1400 cm$^{-1}$ suggesting elimination of OH groups. According to Zhou et al., under subcritical water conditions, acid-catalyzed de-hydration is the main reaction experienced by GO at low concentrations [89]. At 180 °C however, the de-hydration effect is less marked. This could be explained by the fact that acid- catalyzed de-hydration has a reverse mechanism: the acid-catalyzed hydration. An increase in temperature also favors an increase in the ionic product of water (K$_W$, proton and hydroxide ion concentration). Therefore, increasing the temperature may favor the hydration reaction over de-hydration.

Inspection of the IR spectra of CNC after HT (refer to CNC HT at 150 °C and 180 °C in Figure 25) reveals the disappearance of the peak at 807 cm$^{-1}$ indicating de-sulfation of CNC. There change in the intensity of the band at 897 cm$^{-1}$ is explained by changes in hydrogen bonding. No significant change in the intensity of the 1428 cm$^{-1}$ to 897 cm$^{-1}$ band ratio is noted, suggesting a preservation of the Cellulose I crystal structure upon HT. Previous studies concluded that below 280 °C, subcritical water is not able to dissolve

crystalline cellulose [90]. Therefore, CNC experiences partial de-sulfation after the HT. De-sulfation of CNC is believed to occur by an acid-catalyzed ester hydrolysis mechanism [91].

The addition of CNC stabilizes the resulting rGO dispersion upon HT (refer to Figure 26). The UV-Visible spectra for the 20:1 CNC/GO case (refer to Figure 27b) reveals an increase in absorbance after HT at 150 °C and 180 °C. However, the increase in absorbance is higher for the dispersion treated at 150 °C. According to the Beer-Lambert law, the increase in absorbance should be a consequence of changes in analyte concentration or absorption coefficient, because the path length remains constant. The concentration should at least be equal or minor than the initial concentration due to possible precipitation. Therefore, the increase in absorbance suggests a restoration of the π-conjugation network within the GO sheets.
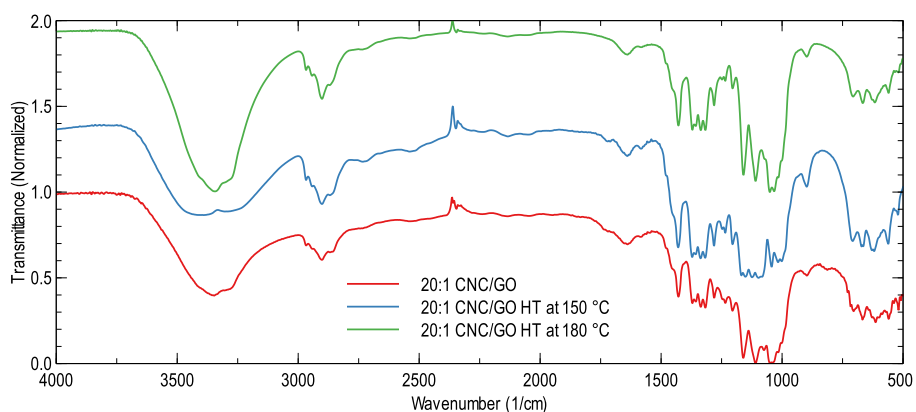


Figure 28 IR spectra of 20:1 CNC/GO

The IR spectra of 20:1 CNC/GO case are compared in Figure 28. The spectra between 20:1 and 20:1 HT at 180 °C do not show major difference except for the evidence of CNC de-sulfation. This resembles the behavior of GO alone with HT temperature (refer to GO HT at 180 °C in Figure 24). Further, the decrease in the absorbance of spectra of 20:1 CNC/GO case HT at 180°C versus the 150°C case indicates that excessive de-sulfation may lead to agglomeration and precipitation of CNC carrying with it GO/rGO. However, comparing the spectrum of 20:1 HT at 150 °C versus untreated 20:1 reveals notorious

changes located between the 1000 cm⁻¹ – 1200 cm⁻¹ region. A de-hydration reaction is suggested by the disappearance of the peak at 1109 cm⁻¹ (C–OH). The population of epoxy groups diminishes upon HT while the population of carboxyl groups increases as detailed in Table 4. These carboxyl groups do not seem to be bounded to rGO because of the lack of the shoulder near 300 nm (n→π∗ transitions of C=O) in the corresponding UV-Visible spectra (refer to 20:1 CNC/GO at 150 °C in Figure 27b). Inspection of the IR spectra of 1:1 and 10:1 CNC/GO cases HT at 150 °C do not reveal the same structural changes noted for 20:1 CNC/GO (refer to Figure 38 and Figure 39). Particularly, no appreciable de-hydration reaction is appreciated for the latter cases.

Table 4 Spectra differences between 1000 cm−1 – 1200 cm−1 region for 20:1 untreated and 20:1 HT at 150 °C

| | Peaks Position (cm−1) | |
| --- | --- | --- |
| Peak Assignment | 20:1 CNC/GO No HT | 20:1 CNC/GO HT 150 °C |
| ν(C-O) from carboxyl | 1160 | 1081, 1043 |
| ν(C-O-C) from epoxy | 1075, 1050 | 1151 |
| ν(C-OH) | 1109 | - |

To further understand the effect of composition, HT temperature and HT time on the effectiveness of the Hydrothermal Treatment, a multifactorial experiment was designed selecting the change in the UV-Vis absorbance of the dispersion at 600nm as a marker for graphene reduction (refer to Figure 29). It is concluded that it is more critical to control temperature and time rather than compositions in order to obtain the largest change in terms of absorbance. As a consequence, for further hydrothermal treatments of GO/CNC dispersions, the temperature is fixed at 150°C and the time at 1.0 hours.
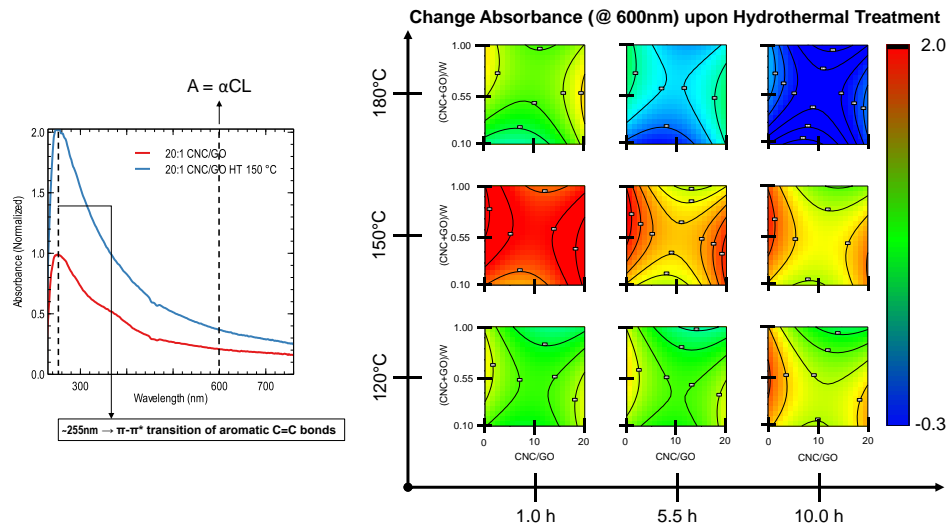
Figure 29 Change in absorbance at 600nm upon hydrothermal treatment of GO/CNC aqueous dispersions

Inspection of the dispersions before and after hydrothermal treatment using AFM technique (refer to Figure 30) reveals that simultaneous restoration of the graphene conjugated structure and partial "desulfation" of the CNC fibers promote the covering of the graphene sheets by the fiber indicating a physical blocking mechanism of the individual sheets preventing the re-stacking of the same.
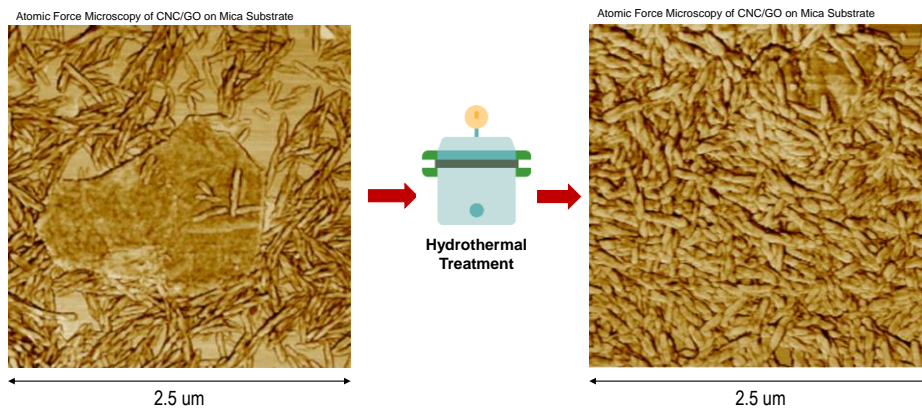


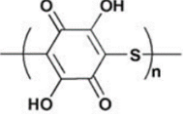Figure 30 AFM scans for 10:1 CNC/GO samples before and after HT at 150°C for 5.5 hours
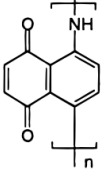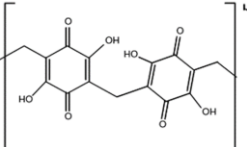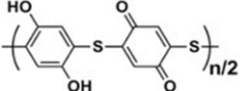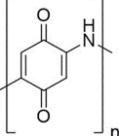
# 7 Polyquinone Core-Shell Structures with Cellulose Nanocrystals and Graphene

## 7.1 Background

In Chapter 5 it was outlined the ability of cellulose nanocrystals to stabilize (avoid restacking) graphene and few-layer graphene aqueous dispersions. Such aqueous dispersion could potentially serve as reaction media for a polymerization reaction. In particular, it would be desirable to promote few-layer graphene sheets coating by a polymer layer, in order to accomplish a core-shell nanocomposite, via a solution-scalable approach, that efficiently increases the contact area between additive and polymer. Therefore, it is investigated the *in-situ* polymerization of an electroactive polymer in cellulose-nanocrystals/graphene aqueous dispersion.

As stated in Chapter 2 and 3, quinone is an attractive candidate for electrochemical energy storage cathodes due to its high redox potential (2.5–3.0 V vs $Li^+$/Li) and theoretical capacity (496 mAh $g^{-1}$). Those properties are superior to current commercial Li-Ion cathodes theoretical capacity: $LiCoO_2$ (274 mAh $g^{-1}$) and $LiFePO_4$ (170 mAh $g^{-1}$). However, reports on polyquinone as an electrode for EES are technically null. The closest study could be the one executed by Foos and coworkers [92], where they highlight the lack of electronic conductivity for the polymer. On the other hand, one can identify a set of studies regarding quinone derivatives for EES (refer to Table 5). Those studies are motivated by the need of reducing the solubility of the polymer in organic solvents. The drawback of this approach is the increased molar mass that could led to a lower theoretical specific capacity.

Table 5 Specific capacity of selected polyquinone derivatives

| Polymer | Initial Capacity | Capacity Retention | Reference |
|---------|------------------|--------------------|-----------|
|  | 300 mAh g$^{-1}$ at 0.02 A/g | 67% after 15 C/D Cycles at 0.02 A/g | [93] |
|  | 150 mAh g$^{-1}$ at 100μA/cm$^2$ | 67% after 100 C/D Cycles at 100μA/cm$^2$ | [94] |
|  | 350 mAh g$^{-1}$ at 0.015 A/g | 53% after 100 C/D Cycles at 0.015 A/g | [95] |
|  | 275 mAh g$^{-1}$ at 0.050 A/g | 86% after 1000 C/D Cycles at 0.050 A/g | [96] |
|  | 290 mAh g$^{-1}$ at 0.016 A/g | 53% after 30 C/D Cycles at 0.016 A/g | [97] |

Based on the aforementioned, it is desirable to evaluate the synthesis of polymeric quinones as a way to retain the intrinsic high specific capacity of the molecule. The drawbacks of high solubility and low electronic conductivity are assessed by the incorporation of polyquinone as a thin layer covering cellulose-nanocrystals/graphene template as described previously.

## 7.2 Experimental Procedure

### 7.2.1 Materials and Reagents

Unless otherwise stated, the chemicals were ACS quality and used as received without further purification.

### 7.2.2 Synthesis of PQ/G/CNC

CNC/G aqueous dispersions were prepared according to the protocol followed in Chapter 5. The CNC/(G+CNC) mass proportion were varied between 0 – 1. $H_2SO_4$ is added to the aqueous dispersion maintaining fixed concentration of 0.025M for all the cases. p-Benzoquinone (pBQ) is then added to the dispersion varying the (CNC+G)/pBQ ratio between 0.05 – 0.10. The mixture is sonicated for 60 minutes and then placed in a muffle oven at 90°C for 10 hours without stirring. The precipitate was cleaned by filtration (Whatman) ten times using DI water and then dried under vacuum at 60°C for 24 hours. Each sample is labeled as XXCNC – YYG, where XX and YY represents the CNC/pBQ and G/pBQ mass fraction percentage, respectively (refer to Figure 31).
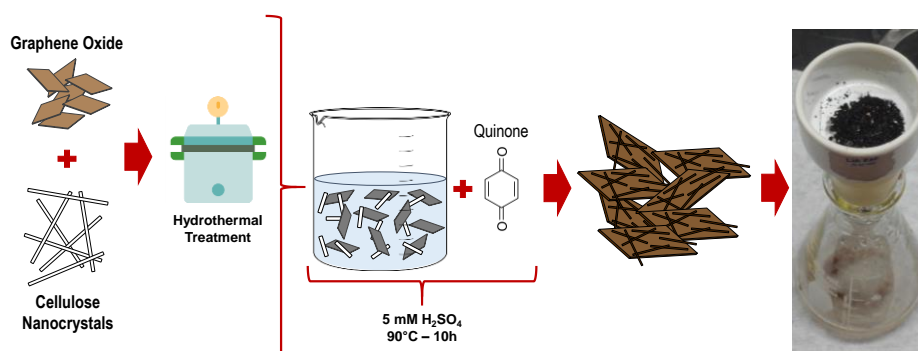


Figure 31 Synthesis protocol for PQ/CNC/GO composites

### 7.2.3 Materials Characterization

For FTIR spectroscopy, the samples were prepared following the KBr pellet method and the spectra recorded on a Jasco FT/IR-6300 Spectrometer (Transmittance Mode). For transmission electron microscopy, the specimen preparation were carried out by drop casting (10 μL) on copper grid 300 mesh, a dispersion of the composite in Acetone (1 mg/mL).

### 7.2.4 Electrode Preparation and Electrochemical Measurements

Graphite sheets were used as current collector for all the tests. A slurry was made consisting on the polyquinone composite as active material, carbon black as conducting agent and Nafion as binder (60:30:10). Nafion is preferred to enhance electrode hydrophilicity and proton conductivity. The slurry is casted on Graphite sheets by the doctor blade technique. The electrodes are dried at 75°C for 6 hours and then at 150°C for 3 hours. The electrodes are immersed overnight in the electrolyte previous electrochemical measurements. All electrochemical tests were performed using a 1M solution of $H_2SO_4$ dissolved in DI water as electrolyte and a three electrode set-up consisting of polymer-modified electrode as working electrode, Saturated Calomel Electrode (SCE) as reference electrode and a graphite rod as counter electrode.

## 7.3 Material Characterization and Analysis

After polymerization, a dark-brown precipitate is appreciated at the bottom of the flask for all the samples (refer to Figure 52). The FTIR spectra suggests the polymerization of pBQ into a co-polymer structure consisting of both benzoquinone and hydroquinone rings for all the samples (refer to Figure 32). The broad band at ~3500 $cm^{-1}$ and the sharp band at ~1200 $cm^{-1}$ associate with the stretching of O-H groups located at phenolic rings. The sharp band at ~1200 $cm^{-1}$ suggests strong intramolecular hydrogen bonding [98]. The band at ~1650 $cm^{-1}$ is assigned to the stretching of C=O groups of quinonoid rings. C-H wagging is suitable for the determination of the type of ring substitution present in benzene derivatives. Particularly, the sharp peak ~815 $cm^{-1}$ is associated to the C−H out of plane bending vibrations of two adjacent hydrogen atoms on a 1,4 disubstituted benzene ring. Therefore, the presence of the additives do not compromise the polymerization reaction. There is no evidence of new bonds besides the characteristic of the polymeric chains. This indicates that the interaction between the polymer and additives could be secondary or Van

der Waals type. The spectral analysis suggest that the mechanism of polymerization of p-Benzoquinone could be represented by Figure 33 [99], [100].
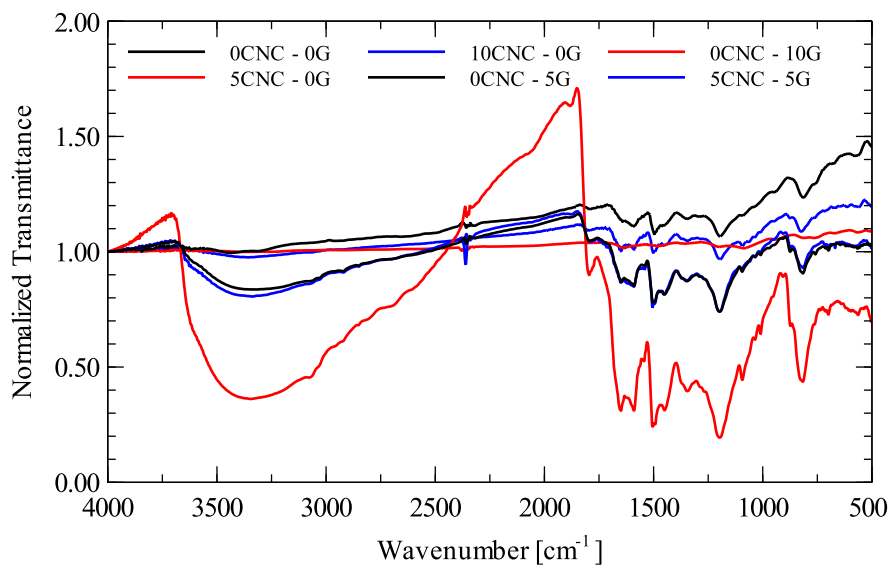


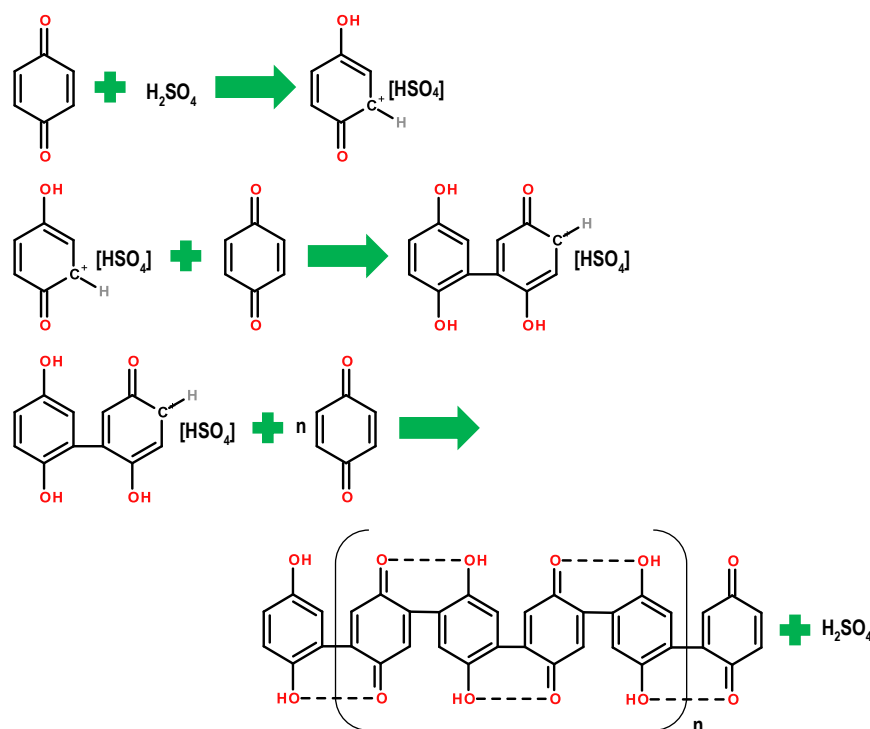Figure 32 FTIR spectra of selected pBQ/CNC/G samples

Figure 33 Polymerization mechanism for p-Benzoquinone

Figure 34a and Figure 34c compares the transmission electron microscopy for sample $0CNC - 5G$ and $5CNC - 5G$, respectively. It is noted that the surface morphology for sample $0CNC - 5G$ seems to be formed by wrinkles while sample $5CNC - 5G$ shows a more flat surface. The electron diffraction pattern shown in Figure 34d for sample $5CNC - 5G$ is associated with that of graphene under normal incidence [101]. For this case, the intensity of [10-10] is stronger than that of [11-20]. The above neglects the presence of ABA… or ABC… stacked Graphene, suggesting the presence of a monolayer. Although the electron diffraction pattern shown in Figure 34d by itself is not a unanimous evidence of monolayer graphene because an AA…A stacking pattern would be possible, reports of AA…A stacked graphite are scarce. For those cases which cellulose is absent (refer to Figure 34b), a few-layer turbostratic stacking electron diffraction pattern is shown. This particular agglomeration could be a result of graphene stacking upon reduction from graphite oxide

in the aqueous media. Therefore, the stabilizing effect of cellulose nanocrystals on graphene dispersions, as reported in chapter 5 is preserved allowing the polymer to coat few-layer graphene sheets.
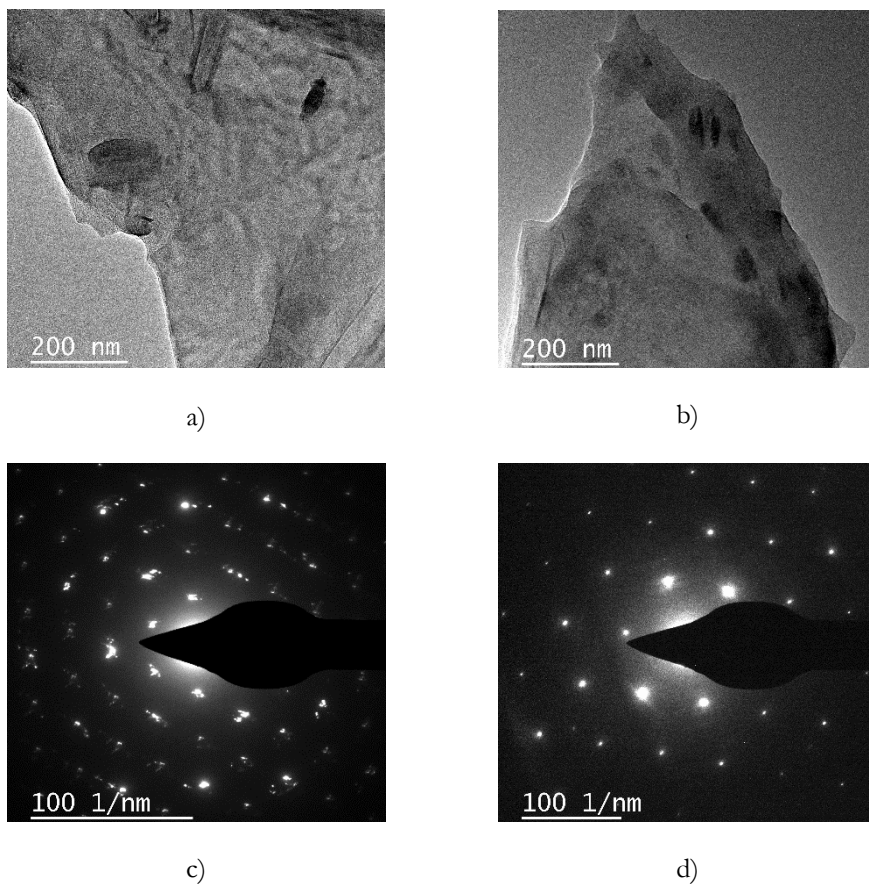


Figure 34 Electron transmission microscopy and electron diffraction pattern for sample 0CNC − 5G (a and b) and sample 5CNC − 5G (c and d)

In aqueous media at acidic pH Quinones are reduced by a single step process involving two-electrons and two-protons generating one reversible wave in the corresponding voltammogram [102] (refer to Figure 35). Cellulose nanocrystals alone seems to make the redox transitions more sluggish as one can notice less resolved peaks as nanofiber content increases. The addition of graphene alone tends to slightly diminish the peak separation indicating an enhancement of the reaction kinetics. However, the peak separation is further

smaller for the 5CNC − 5G case which indicates that the redox kinetics strongly benefits from the more efficient exploitation of graphene by the presence of cellulose nanocrystals.
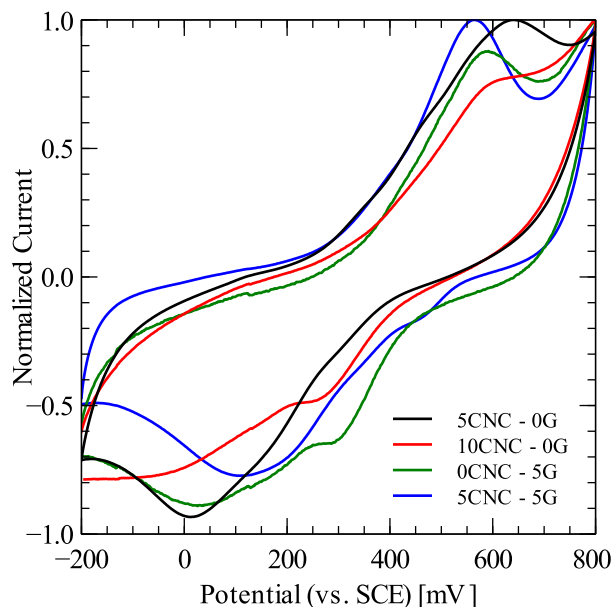


Figure 35 Cyclic voltammogram at 5mV/s for selected samples in 1M $H_2SO_4$

The specific capacity of the resulting composites is evaluated by galvanostatic charge/discharge technique at 0.1 A/g before and after 50 cycles (refer to Figure 36). The sole incorporation of graphene offers limited improvement regarding specific capacity, 52.2 mAh $g^{-1}$, and capacity retention, 66.2%. However, it is worth noting that the addition of cellulose nanocrystals offers significant improvement on electrochemical performance. For the 5CNC − 5G sample, the specific capacitance reaches 100.7 mAh $g^{-1}$ and the capacitance retention is 98.2% after 50 cycles of charge/discharge. This results once again suggest that the stabilization effect of cellulose nanocrystals allows a more efficient exploitation of the graphene sheets. Although the capacity reported is quite below those values obtained for different polyquinone derivatives (refer to Table 5), the rate capability of the resulting material is higher as the charge/discharge were performed at 0.1 A/g. That is, the material performed satisfactory (in terms of capacity and stability) at current rates of one order of magnitude higher than the current typically used for organic electrode characterization.
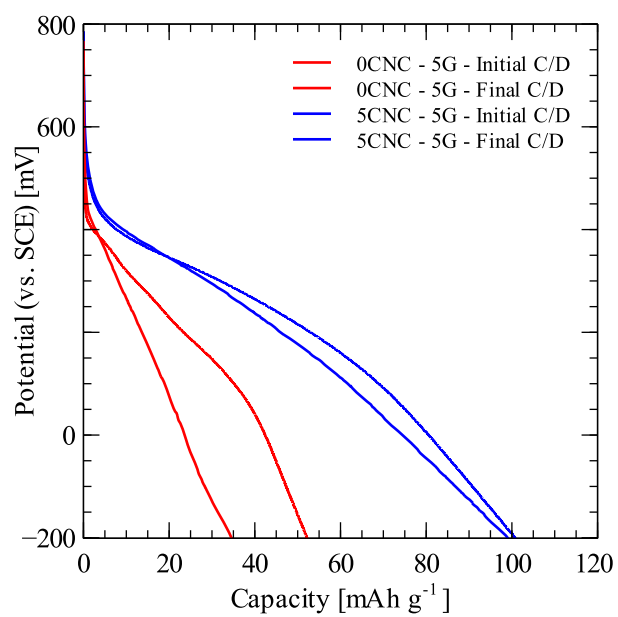
Figure 36 Specific capacitance for selected pBQ/CNC/G samples

# 8 Conclusions

In summary, the work carried out and presented herein has focused on the **solution-based** synthesis of **polymer-based composite** electrodes for EES as a suitable option against traditional inorganic based materials. Emphasis have been placed on the need to incorporate **sustainability measures** during the process in order to meet the current and future role of EES devices in society. To do so, the design principles defined for the synthesis process included, among others, the need to use **aqueous reaction media**, incorporation of **low-cost** and **bio-mass** derived feedstocks to the electrode fabrication process, avoidance of **critical materials**, and maintaining the temperature of the individual processes below **250°C**. The main result is that the **electrochemical performance** of the nanocomposite materials **surpass** that of the polymer-based versions of the same. This is of paramount importance for the EES field because it proves that significant improvements could be obtained by efficient and rational exploitation of relative simple and solution-scalable processing.

The synthesis of cross-linked PANI/G/ND nanocomposites was performed following a low-cost/high-volume (industrial scalable) methodology. The presence of G and ND during the oxidative polymerization of aniline does not interfere the formation of polyaniline (emeraldine base) with a predominating linear structure (para-coupling). The microstructure of the nanocomposites is core-shell with the fillers being wrapped by PANI. A porous 3D network is created by nano-diamond-coated particles working as spacers for graphene-coated sheets. The electroactivity of the nanocomposites has a major contribution by the characteristic redox reactions of the conjugated polymer and only a minor contribution from the double-layer charging is observed. By adjusting the aniline-to-filler ratio the stability and electrochemical performance of the nanocomposite materials is positively affected relative to pristine PANI as evidenced by (a) a maximum delay in the temperature of decomposition of ~13°C, (b) a positive shift in the peak temperature of

crosslinking by a maximum of ~88°C, (c) a reported increase in the gravimetric capacitance by a maximum of 120% and (d) a capacitance retention of 87% after charge/discharge at 1 A/g and a potential window of 2500 mV

Electrochemical characterization were performed on in-situ-formed films during chemical polymerization of aniline in the presence of a nano-crystalline cellulose whiskers suspension. The films are envisioned as active materials for electrochemical energy storage technologies incorporating sustainability measures. Early results suggest a possible template role for nano-crystalline cellulose in the resulting polyaniline/CNC nanocomposite. By template role it is understood as the effect of a morphological control due the coating of CNC whiskers by polyaniline. The whisker-like possible structure allows more surface area in contact with the electrolyte, boosting charge transport reactions and increasing electroactive regions. Electrochemical performance is optimized by adjusting the mass proportion of the corresponding precursors.

Stable aqueous dispersions of rGO were obtained by hydrothermal reduction of GO dispersions in the presence of CNC. Specifically, the dispersion consisting on a CNC/GO mass ratio of 20 subjected to hydrothermal treatment at 150 °C for 10 hours, registered the highest degree of GO reduction. The mechanism of reduction seems to be associated with an acid-catalyzed de-hydration reaction of GO hydroxyl functional groups. There is no evidence of removal of C-O groups from GO. However, spectroscopy analysis suggests the predominance of G conjugated structure, indicating the low-defect quality of rGO. Simultaneous de-sulfation of CNC is evidenced and possibly occurring by an acid-catalyzed ester hydrolysis mechanism. Nevertheless, the remaining sulfate half-ester functional groups on CNC allow stabilization of CNC/rGO dispersions.

p-Benzoquinone was cationically polymerized in a dilute (25mM) $H_2SO_4$ aqueous solution containing cellulose-nanocrystals stabilized graphene. The restacking-prevention effect of cellulose nanocrystals discussed in Chapter 5 significantly enhanced the efficiency

of graphene as a conductive additive to improve the electrochemical performance of polyquinone electrodes. Precisely, during polymerization pBQ molecules were able to coat mono to few-layer graphene sheets. The specific capacitance of the 5CNC − 5G reached 100.7 mAh g$^{-1}$ at 0.1 A/g. Further, 98.2% of the initial capacity were preserved after 50 cycles at 0.1 A/g.

# 9 Further Research Activities

Several tasks remain to be solved in order to further improve the synthesis and performance of current developed materials. Particularly, the following activities must be carried out:

- **Life-cycle** assessment of synthetic routes in order to identify possible pitfalls and new opportunities of improvement regarding sustainable material production.

- **Long-term performance** characterization of EES devices manufactured with the developed nanocomposites and exposed to different ambient conditions.

- Exploration of new and sustainable ways to **derive aniline-** and **quinone-** based polymer from **biomass feedstocks**.

# 10 Appendix

## 10.1 Appendix from Chapter 4

Table 6 ANOVA for Temperature of Decomposition

| Source of Variation | Sum of Squares | Degree of Freedom | Mean Square | $F_o$ | P-Value |
|---|---|---|---|---|---|
| G | 219.2 | 2 | 109.6 | 404.2 | $2.4 \cdot 10^{-5}$ |
| ND | 8.6 | 2 | 4.3 | 15.9 | $1.3 \cdot 10^{-2}$ |
| Error | 1.1 | 4 | 0.3 | | |
| Total | 228.8 | 8 | | | |

Table 7 ANOVA for Peak Crosslinking Temperature

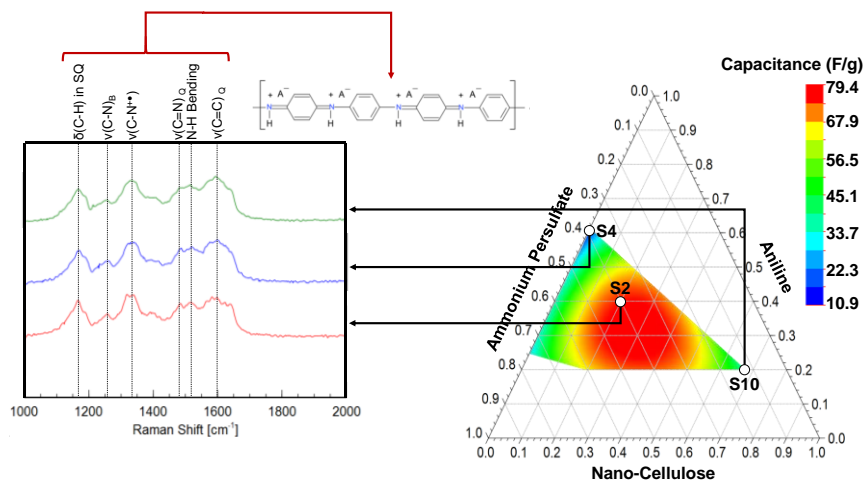| Source of Variation | Sum of Squares | Degree of Freedom | Mean Square | $F_o$ | P-Value |
|---|---|---|---|---|---|
| G | 6195.7 | 2 | 3097.8 | 226.5 | $7.7 \cdot 10^{-5}$ |
| ND | 1150.4 | 2 | 575.2 | 42.1 | $2.1 \cdot 10^{-3}$ |
| Error | 54.7 | 4 | 13.7 | | |
| Total | 7400.7 | 8 | | | |

## 10.2 Appendix from Chapter 5



Figure 37 Raman spectra of selected PANI/CNC samples
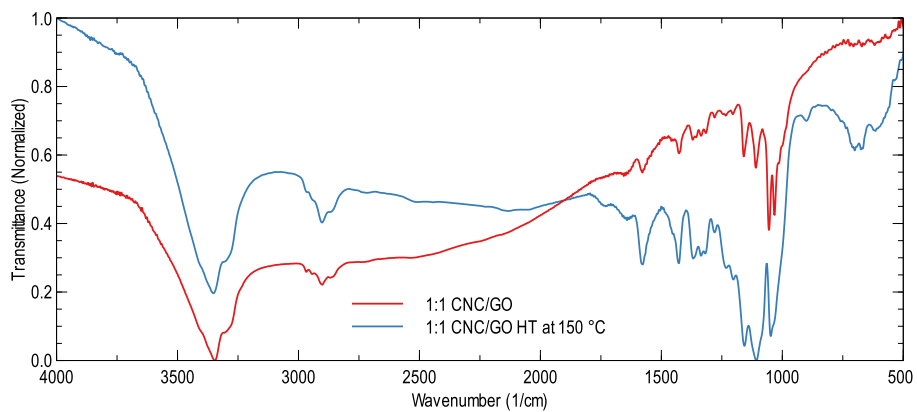
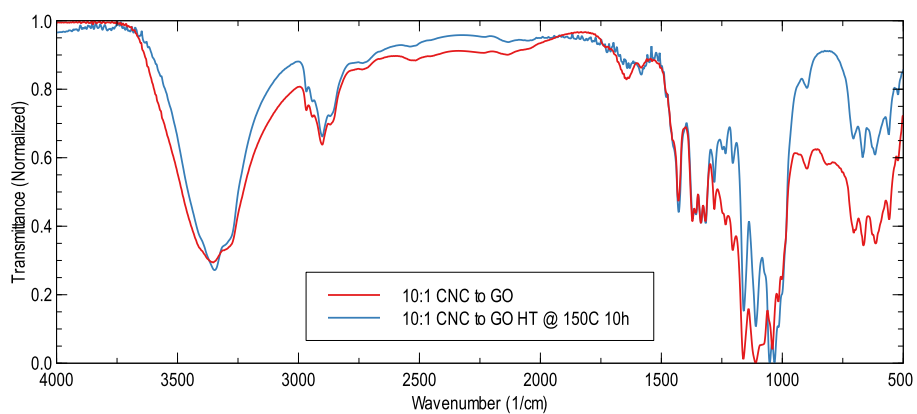## 10.3 Appendix from Chapter 6



Figure 38 IR spectra of 1:1 CNC/GO



Figure 39 IR spectra of 10:1 CNC/GO



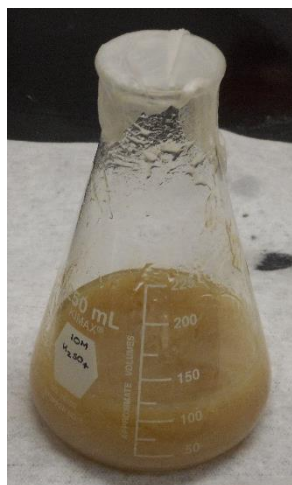Figure 40 100ml of 10 M $H_2SO_4$ and 10g Cotton prior to CNC Extraction

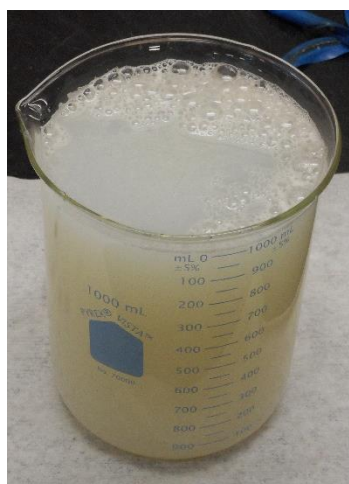Figure 41 Cotton + 10 M $H_2SO_4$ after reaction at 50°C for 1h



Figure 42 Cotton + 10 M $H_2SO_4$ after reaction at 50°C for 1h and 10x diluted with $H_2O$
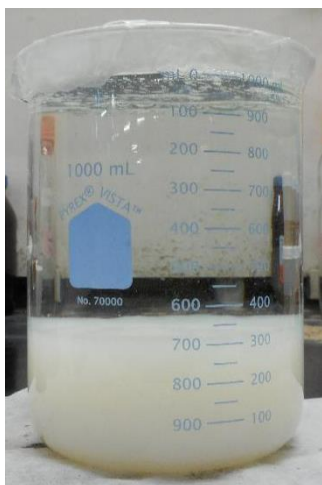
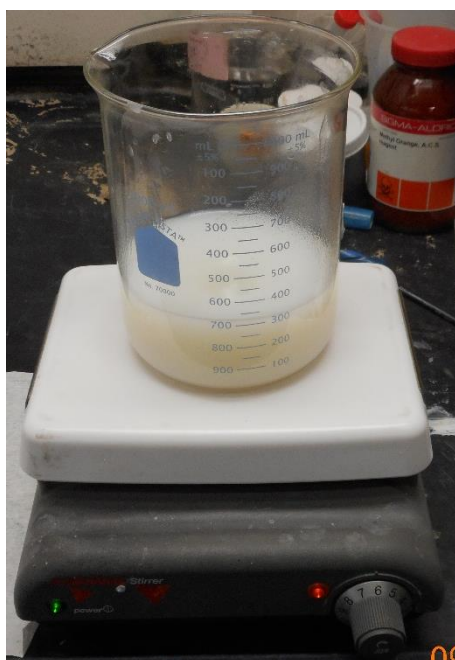Figure 43 Cotton + 10 M $H_2SO_4$ after reaction at 50°C for 1h and 10x diluted with $H_2O$ (24 h of rest)



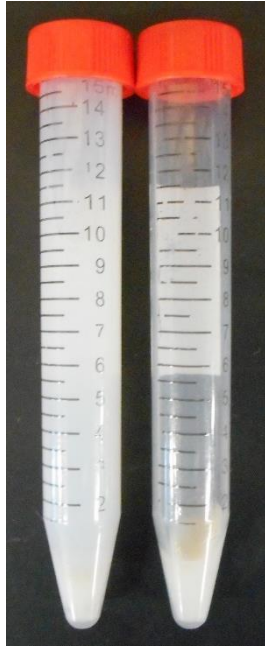Figure 44 Homogenization of precipitated hydrolyzed cellulose

Figure 45 Comparison of CNC colloidal dispersion (left) and precipate (right) during cleaning by centrifugation

## 10.4 Appendix from Chapter 7



Figure 46 From left to right, 5CNC – 0G sample filtrate from each step, after 30 min of centrifugation



Figure 47 From left to right, 0CNC – 5G sample filtrate from each step, after 30 min of centrifugation
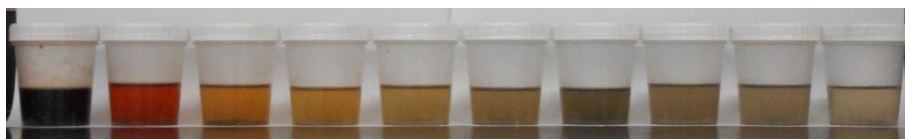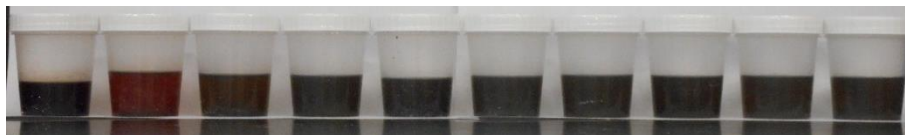


Figure 48 From left to right, 0CNC – 10G sample filtrate from each step, after 30 min of centrifugation
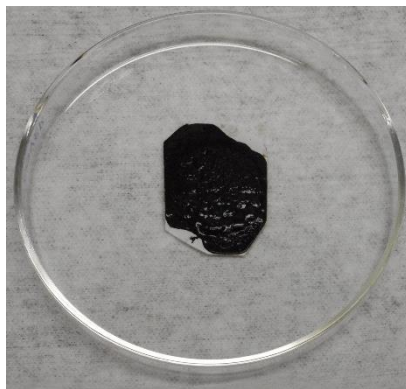


Figure 49 10CNC – 0G sample after filtering prior to drying
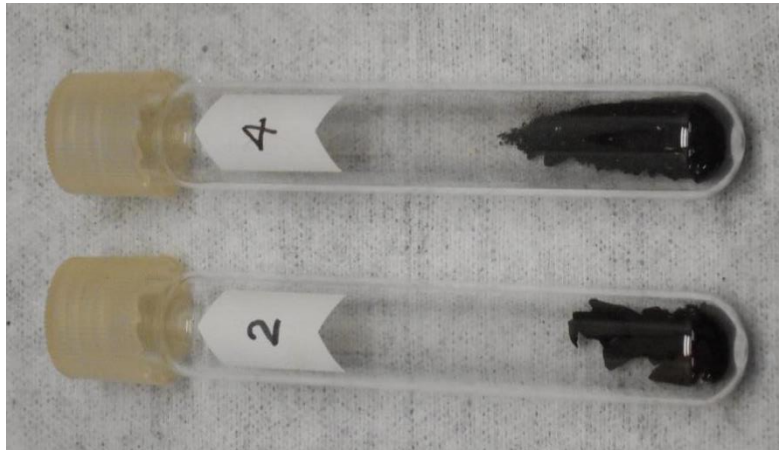
Figure 50 5CNC – 0G (2) and 0CNC – 0G (4) sample after drying



Figure 51 10CNC – 0G sample reaction container after reaction

Figure 52 0CNC – 0G sample during filtration. Notice the brittle appearance of the polymer.

## 10.5 List of Equipment

| | |
|---|---|
| Name: Scanning Electron Microscope<br>Model: JEOL JSM 5600<br>Location: Universidad del Norte |  |
| Name: Potentiostat<br>Model: Voltalab® PGZ301<br>Location: Universidad del Norte |  |
| Name: Balance<br>Model: Precisa® 180ª<br>Location: Universidad del Norte |  |
| Name: Magnetic Stirrer<br>Model: VWR® Dylastir®<br>Location: Universidad del Norte |  |

| | |
|---|---|
| Name: IR Spectrophotometer<br>Model: Shimadzu IR Prestige-21<br>Location: Universidad Pedagógica de Tunja |  |
| Name: TGA/DSC<br>Model: STD-Q600<br>Location: Universidad Pedagógica de Tunja |  |
| Name: Centrifuge<br>Model: Fisher Scientific Centrific 228<br>Location: CERC – University of South Florida |  |
| Name: Balance<br>Model: Ohaus Adventurer 3130<br>Location: CERC – University of South Florida |  |
| Name: Muffle Furnace<br>Model: Neycraft Vulcan 3-550<br>Location: CERC – University of South Florida |  |

| | |
|---|---|
| Name: UV-Visible Spectrophotometer<br>Model: Ocean Optics USB2000<br>Location: CERC – University of South Florida |  |
| Name: IR Spectrophotometer<br>Model: Jasco FT/IR-6300<br>Location: CERC – University of South Florida |  |
| Name: Vacuum Oven<br>Model: Fisher Scientific Isotemp 280A<br>Location: CERC – University of South Florida |  |
| Name: DC Power Source<br>Model: Agilent E3640A<br>Location: CERC – University of South Florida |  |
| Name: Transmission Electron Microscope<br>Model: FEI Tecnai G2-F20<br>Location: Universidad de Antioquia |  |

| | |
|---|---|
| Name: Atomic Force Microscope<br>Model: Veeco Dimension 3000<br>Location: NRC – University of South Florida |  |
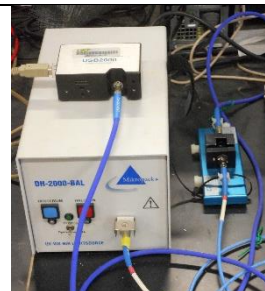
# 11 References

[1]     J. F. Peters, M. Baumann, B. Zimmermann, J. Braun, and M. Weil, "The environmental impact of Li-Ion batteries and the role of key parameters – A review," *Renew. Sustain. Energy Rev.*, vol. 67, pp. 491–506, Jan. 2017.

[2]     K. Richa, C. W. Babbitt, G. Gaustad, and X. Wang, "A future perspective on lithium-ion battery waste flows from electric vehicles," *Resour. Conserv. Recycl.*, vol. 83, pp. 63–76, Feb. 2014.

[3]     H. Vikström, S. Davidsson, and M. Höök, "Lithium availability and future production outlooks," *Appl. Energy*, vol. 110, pp. 252–266, Oct. 2013.

[4]     B. Swain, "Recovery and recycling of lithium: A review," *Sep. Purif. Technol.*, vol. 172, pp. 388–403, Jan. 2017.

[5]     P. Poizot and F. Dolhem, "Clean energy new deal for a sustainable world: from non-$CO_2$ generating energy sources to greener electrochemical storage devices," *Energy Environ. Sci.*, vol. 4, no. 6, p. 2003, 2011.

[6]     D. Larcher and J.-M. Tarascon, "Towards greener and more sustainable batteries for electrical energy storage.," *Nat. Chem.*, vol. 7, no. 1, pp. 19–29, 2015.

[7]     P. T. Anastas and J. C. Warner, *Green Chemistry: Theory and Practice*. Oxford University Press, 2000.

[8]     P. T. Anastas and J. B. Zimmerman, "Peer Reviewed: Design Through the 12 Principles of Green Engineering," *Environ. Sci. Technol.*, vol. 37, no. 5, pp. 94A-101A, 2003.

[9]     M. Arbabzadeh, J. X. Johnson, G. a Keoleian, P. G. Rasmussen, and L. T. Thompson, "Twelve Principles for Green Energy Storage in Grid Applications.," *Environ. Sci. Technol.*, vol. 50, no. 2, pp. 1046–55, 2016.

[10]    A. J. Hurd, R. L. Kelley, R. G. Eggert, and M.-H. Lee, "Energy-critical elements for sustainable development," *MRS Bull.*, vol. 37, no. 4, pp. 405–410, 2012.

[11]    I. Lubomirsky and D. Cahen, "Energy limitations on materials availability," *MRS Bull.*, vol. 37, no. 04, pp. 412–416, 2012.

[12] T. G. Gutowski, S. Sahni, J. M. Allwood, M. F. Ashby, and E. Worrell, "The energy required to produce materials: constraints on energy-intensity improvements, parameters of demand," *Philos. Trans. R. Soc. A Math. Phys. Eng. Sci.*, vol. 371, no. 1986, pp. 20120003–20120003, Jan. 2013.

[13] N. J. van Eck and L. Waltman, "Software survey: VOSviewer, a computer program for bibliometric mapping," *Scientometrics*, vol. 84, no. 2, pp. 523–538, Aug. 2010.

[14] R. Bailón-Moreno, E. Jurado-Alameda, R. Ruiz-Baños, and J. P. Courtial, "Bibliometric laws: Empirical flaws of fit," *Scientometrics*, vol. 63, no. 2, pp. 209–229, Apr. 2005.

[15] G. Chen and L. Xiao, "Selecting publication keywords for domain analysis in bibliometrics: A comparison of three methods," *J. Informetr.*, vol. 10, no. 1, pp. 212–223, Feb. 2016.

[16] S. Lee *et al.*, "Recent Progress in Organic Electrodes for Li and Na Rechargeable Batteries," *Adv. Mater.*, vol. 30, no. 42, p. 1704682, Oct. 2018.

[17] C. Stolze, T. Janoschka, S. Flauder, F. A. Müller, M. D. Hager, and U. S. Schubert, "Investigation of Ice-Templated Porous Electrodes for Application in Organic Batteries," *ACS Appl. Mater. Interfaces*, vol. 8, no. 36, pp. 23614–23623, Sep. 2016.

[18] D. Li *et al.*, "Synthesis of ternary graphene/molybdenum oxide/poly(p-phenylenediamine) nanocomposites for symmetric supercapacitors," *RSC Adv.*, vol. 5, no. 119, pp. 98278–98287, 2015.

[19] J. Li, Y. Sun, D. Li, H. Yang, X. Zhang, and B. Lin, "Novel ternary composites reduced-graphene oxide/zinc oxide/poly(p-phenylenediamine) for supercapacitor: Synthesis and properties," *J. Alloys Compd.*, vol. 708, pp. 787–795, Jun. 2017.

[20] A. Moyseowicz, A. Śliwak, E. Miniach, and G. Gryglewicz, "Polypyrrole/iron oxide/reduced graphene oxide ternary composite as a binderless electrode material with high cyclic stability for supercapacitors," *Compos. Part B Eng.*, vol. 109, pp. 23–29, Jan. 2017.

[21] M. Armand *et al.*, "Conjugated dicarboxylate anodes for Li-ion batteries," *Nat. Mater.*, vol. 8, no. 2, pp. 120–125, Feb. 2009.

[22]    L. Yang, X. Huang, A. Gogoll, M. Strømme, and M. Sjödin, "Conducting Redox Polymer Based Anode Materials for High Power Electrical Energy Storage," *Electrochim. Acta*, vol. 204, pp. 270–275, Jun. 2016.

[23]    L. Yang, X. Huang, A. Gogoll, M. Strømme, and M. Sjödin, "Effect of the Linker in Terephthalate-Functionalized Conducting Redox Polymers," *Electrochim. Acta*, vol. 222, pp. 149–155, Dec. 2016.

[24]    C. Chen, X. Li, F. Deng, and J. Li, "Electropolymerization and electrochemical behavior of nickel Schiff base complexes with different groups between imine linkages," *RSC Adv.*, vol. 6, no. 83, pp. 79894–79899, 2016.

[25]    E. V. Alekseeva, I. A. Chepurnaya, V. V. Malev, A. M. Timonov, and O. V. Levin, "Polymeric nickel complexes with salen-type ligands for modification of supercapacitor electrodes: impedance studies of charge transfer and storage properties," *Electrochim. Acta*, vol. 225, pp. 378–391, Jan. 2017.

[26]    X. Li, F. Deng, J. Li, Z. Li, and F. Kang, "Fast and reversible redox reaction of polyNi(salphen)@reduced graphene oxide/multiwall carbon nanotubes composite for supercapacitors," *Electrochim. Acta*, vol. 284, pp. 355–365, Sep. 2018.

[27]    A. A. Vereshchagin, P. S. Vlasov, A. S. Konev, P. Yang, G. A. Grechishnikova, and O. V. Levin, "Novel highly conductive cathode material based on stable-radical organic framework and polymerized nickel complex for electrochemical energy storage devices," *Electrochim. Acta*, vol. 295, pp. 1075–1084, Feb. 2019.

[28]    "Covestro pursues biobased aniline," *C&EN Glob. Enterp.*, vol. 95, no. 23, pp. 10–10, Jun. 2017.

[29]    I. Abraham, R. Joshi, P. Pardasani, and R. . Pardasani, "Recent advances in 1,4-benzoquinone chemistry," *J. Braz. Chem. Soc.*, vol. 22, no. 3, pp. 385–421, Mar. 2011.

[30]    Y. Shi, L. Peng, Y. Ding, Y. Zhao, and G. Yu, "Nanostructured conductive polymers for advanced energy storage," *Chem. Soc. Rev.*, vol. 44, no. 19, pp. 6684–6696, 2015.

[31]    Y.-E. Miao, W. Fan, D. Chen, and T. Liu, "High-performance supercapacitors based on hollow polyaniline nanofibers by electrospinning.," *ACS Appl. Mater. Interfaces*, vol. 5,

no. 10, pp. 4423–8, 2013.

[32]     G. Inzelt, "Redox Transformations and Transport Processes," Springer Berlin Heidelberg, 2012, pp. 191–244.

[33]     K. Zhang, L. L. Zhang, X. S. Zhao, and J. Wu, "Graphene/Polyaniline Nanofiber Composites as Supercapacitor Electrodes," *Chem. Mater.*, vol. 22, no. 4, pp. 1392–1401, Feb. 2010.

[34]     N. A. Kumar, H.-J. Choi, Y. R. Shin, D. W. Chang, L. Dai, and J.-B. Baek, "Polyaniline-grafted reduced graphene oxide for efficient electrochemical supercapacitors.," *ACS Nano*, vol. 6, no. 2, pp. 1715–23, Feb. 2012.

[35]     J. Zhang and X. S. Zhao, "Conducting polymers directly coated on reduced graphene oxide sheets as high-performance supercapacitor electrodes," *J. Phys. Chem. C*, vol. 116, no. 9, pp. 5420–5426, 2012.

[36]     H. Gómez, M. K. Ram, F. Alvi, P. Villalba, E. (Lee) Stefanakos, and A. Kumar, "Graphene-conducting polymer nanocomposite as novel electrode for supercapacitors," *J. Power Sources*, vol. 196, no. 8, pp. 4102–4108, Apr. 2011.

[37]     Z.-F. Li, H. Zhang, Q. Liu, L. Sun, L. Stanciu, and J. Xie, "Fabrication of high-surface-area graphene/polyaniline nanocomposites and their application in supercapacitors.," *ACS Appl. Mater. Interfaces*, vol. 5, no. 7, pp. 2685–91, Apr. 2013.

[38]     M. Kim, C. Lee, and J. Jang, "Fabrication of highly flexible, scalable, and high-performance supercapacitors using polyaniline/reduced graphene oxide film with enhanced electrical conductivity and crystallinity," *Adv. Funct. Mater.*, vol. 24, no. 17, pp. 2489–2499, 2014.

[39]     A. K. Sarker and J. D. Hong, "Layer-by-Layer self-assembled multilayer films composed of graphene/polyaniline bilayers: High-Energy electrode materials for supercapacitors," *Langmuir*, vol. 28, no. 34, pp. 12637–12646, 2012.

[40]     J. Yan *et al.*, "Preparation of a graphene nanosheet/polyaniline composite with high specific capacitance," *Carbon N. Y.*, vol. 48, no. 2, pp. 487–493, 2010.

[41]     W. Fan, C. Zhang, W. W. Tjiu, K. P. Pramoda, C. He, and T. Liu, "Graphene-wrapped

polyaniline hollow spheres as novel hybrid electrode materials for supercapacitor applications.," *ACS Appl. Mater. Interfaces*, vol. 5, no. 8, pp. 3382–91, Apr. 2013.

[42] X. Liu, N. Wen, X. Wang, and Y. Zheng, "A High-Performance Hierarchical Graphene@Polyaniline@Graphene Sandwich Containing Hollow Structures for Supercapacitor Electrodes," *ACS Sustain. Chem. Eng.*, vol. 3, no. 3, pp. 475–482, Mar. 2015.

[43] V. N. Mochalin, O. Shenderova, D. Ho, and Y. Gogotsi, "The properties and applications of nanodiamonds.," *Nat. Nanotechnol.*, vol. 7, no. 1, pp. 11–23, Jan. 2012.

[44] M. Yoshimura *et al.*, "Electrochemical characterization of nanoporous honeycomb diamond electrodes in non-aqueous electrolytes," *Diam. Relat. Mater.*, vol. 10, no. 3–7, pp. 620–626, Mar. 2001.

[45] K. B. Holt *et al.*, "Redox properties of undoped 5 nm diamond nanoparticles," *Phys. Chem. Chem. Phys.*, vol. 10, no. 2, pp. 303–310, 2008.

[46] H. Gomez, M. K. Ram, F. Alvi, E. Stefanakos, and A. Kumar, "Novel Synthesis, Characterization, and Corrosion Inhibition Properties of Nanodiamond−Polyaniline Films," *J. Phys. Chem. C*, vol. 114, no. 44, pp. 18797–18804, Nov. 2010.

[47] I. Kovalenko, D. G. Bucknall, and G. Yushin, "Detonation Nanodiamond and Onion-Like-Carbon-Embedded Polyaniline for Supercapacitors," *Adv. Funct. Mater.*, vol. 20, no. 22, pp. 3979–3986, Nov. 2010.

[48] R. Raccichini, A. Varzi, S. Passerini, and B. Scrosati, "The role of graphene for electrochemical energy storage.," *Nat. Mater.*, vol. 14, no. 3, pp. 271–9, 2015.

[49] G. Socrates, *Infrared and Raman Characteristic Group Frequencies: Tables and Charts*. John Wiley & Sons, 2004.

[50] M.-I. Boyer *et al.*, "Vibrational Analysis of Polyaniline: A Model Compound Approach," *J. Phys. Chem. B*, vol. 102, no. 38, pp. 7382–7392, Sep. 1998.

[51] V. Y. Dolmatov, "Detonation-synthesis nanodiamonds: synthesis, structure, properties and applications," *Russ. Chem. Rev.*, vol. 76, no. 4, pp. 339–360, Apr. 2007.

[52] J. Stejskal, I. Sapurina, and M. Trchová, "Polyaniline nanostructures and the role of

aniline oligomers in their formation," *Prog. Polym. Sci.*, vol. 35, no. 12, pp. 1420–1481, Dec. 2010.

[53]    S.-J. Tang *et al.*, "Polymerization of aniline under various concentrations of APS and HCl," *Polym. J.*, vol. 43, no. 8, pp. 667–675, 2011.

[54]    Q. Zou, M. Z. Wang, and Y. G. Li, "Analysis of the nanodiamond particle fabricated by detonation," *J. Exp. Nanosci.*, vol. 5, no. 4, pp. 319–328, Aug. 2010.

[55]    A. Kumar, P. Ann Lin, A. Xue, B. Hao, Y. Khin Yap, and R. M. Sankaran, "Formation of nanodiamonds at near-ambient conditions via microplasma dissociation of ethanol vapour," *Nat. Commun.*, vol. 4, no. 1, p. 2618, Dec. 2013.

[56]    L. Ding, X. Wang, and R. . Gregory, "Thermal properties of chemically synthesized polyaniline (EB) powder," *Synth. Met.*, vol. 104, no. 2, pp. 73–78, Jul. 1999.

[57]    W. F. Alves *et al.*, "Thermo-analyses of polyaniline and its derivatives," *Thermochim. Acta*, vol. 502, no. 1–2, pp. 43–46, Apr. 2010.

[58]    M. E. G. Lyons, *Electroactive Polymer Electrochemistry, Volume 1.* Springer, 1994.

[59]    S. Park and R. S. Ruoff, "Chemical methods for the production of graphenes.," *Nat. Nanotechnol.*, vol. 4, no. 4, pp. 217–24, Apr. 2009.

[60]    D. C. Montgomery, *Design and Analysis of Experiments*. 2008.

[61]    A. Leszczyńska, J. Njuguna, K. Pielichowski, and J. R. Banerjee, "Polymer/montmorillonite nanocomposites with improved thermal properties," *Thermochim. Acta*, vol. 453, no. 2, pp. 75–96, Feb. 2007.

[62]    S. Morimune, T. Nishino, and T. Goto, "Poly(vinyl alcohol)/graphene oxide nanocomposites prepared by a simple eco-process," *Polym. J.*, vol. 44, no. 10, pp. 1056–1063, 2012.

[63]    P. Podsiadlo *et al.*, "Ultrastrong and Stiff Layered Polymer Nanocomposites," *Science*, vol. 318, no. October, pp. 1–4, 2007.

[64]    E. Roumeli, E. Pavlidou, A. Avgeropoulos, G. Vourlias, D. N. Bikiaris, and K. Chrissafis, "Factors controlling the enhanced mechanical and thermal properties of nanodiamond-reinforced cross-linked high density polyethylene.," *J. Phys. Chem. B*, vol.

118, no. 38, pp. 11341–52, Sep. 2014.

[65]    R. Wang, L. Huang, and X. Tian, "Understanding the Protonation of Polyaniline and Polyaniline − Graphene Interaction," *J. Phys. Chem. C*, vol. 116, pp. 13120–13126, 2012.

[66]    A. Kabumoto, K. Shinozaki, K. Watanabe, and N. Nishikawa, "Electrochemical degradation of polyaniline," *Synth. Met.*, vol. 26, no. 4, pp. 349–355, Nov. 1988.

[67]    N. Pekmez, K. Pekmez, and A. Yıldız, "Electrochemical behavior of polyaniline films in acetonitrile," *J. Electroanal. Chem.*, vol. 370, no. 1–2, pp. 223–229, Jun. 1994.

[68]    P. Lu and Y.-L. Hsieh, "Preparation and properties of cellulose nanocrystals: Rods, spheres, and network," *Carbohydr. Polym.*, vol. 82, no. 2, pp. 329–336, Sep. 2010.

[69]    A. Ivanova, K. Fominykh, D. Fattakhova-rohl, P. Zeller, M. Do, and T. Bein, "Nanocellulose-Assisted Formation of Porous Hematite Nanostructures," 2014.

[70]    J. Wang, J. Polleux, J. Lim, and B. Dunn, "Pseudocapacitive Contributions to Electrochemical Energy Storage in TiO2 (Anatase) Nanoparticles," *J. Phys. Chem. C*, vol. 111, no. 40, pp. 14925–14931, 2007.

[71]    S. Zhang and N. Pan, "Supercapacitors performance evaluation," *Adv. Energy Mater.*, vol. 5, no. 6, pp. 1–19, 2015.

[72]    Y. Zhu, H. Ji, H.-M. Cheng, and R. S. Ruoff, "Mass production and industrial applications of graphene materials," *Natl. Sci. Rev.*, vol. 5, no. 1, pp. 90–101, Jan. 2018.

[73]    M. Ayán-Varela, J. I. Paredes, S. Villar-Rodil, R. Rozada, A. Martínez-Alonso, and J. M. D. Tascón, "A quantitative analysis of the dispersion behavior of reduced graphene oxide in solvents," *Carbon N. Y.*, vol. 75, pp. 390–400, Aug. 2014.

[74]    D. Li, M. B. Müller, S. Gilje, R. B. Kaner, and G. G. Wallace, "Processable aqueous dispersions of graphene nanosheets," *Nat. Nanotechnol.*, vol. 3, no. 2, pp. 101–105, Feb. 2008.

[75]    Y. Wei and Z. Sun, "Liquid-phase exfoliation of graphite for mass production of pristine few-layer graphene," *Curr. Opin. Colloid Interface Sci.*, vol. 20, no. 5–6, pp. 311–321, Oct. 2015.

[76]    J. Cao *et al.*, "Two-Step Electrochemical Intercalation and Oxidation of Graphite for the

Mass Production of Graphene Oxide," *J. Am. Chem. Soc.*, vol. 139, no. 48, pp. 17446–17456, Dec. 2017.

[77]    S. P. Sasikala, P. Poulin, and C. Aymonier, "Advances in Subcritical Hydro-/Solvothermal Processing of Graphene Materials," *Adv. Mater.*, vol. 29, no. 22, p. 1605473, Jun. 2017.

[78]    D. Illera, V. Fontalvo, and H. Gomez, "Cellulose Nanocrystals Assisted Preparation of Electrochemical Energy Storage Electrodes," in *Volume 14: Emerging Technologies; Materials: Genetics to Structures; Safety Engineering and Risk Analysis*, 2017, p. V014T11A032.

[79]    V. Ţucureanu, A. Matei, and A. M. Avram, "FTIR Spectroscopy for Carbon Family Study," *Crit. Rev. Anal. Chem.*, vol. 46, no. 6, pp. 502–520, Nov. 2016.

[80]    M. Ioelovich, "Characterization of Various Kinds of Nanocellulose," in *Handbook of Nanocellulose and Cellulose Nanocomposites*, Weinheim, Germany: Wiley-VCH Verlag GmbH & Co. KGaA, 2017, pp. 51–100.

[81]    P. Garside and P. Wyeth, "Identification of Cellulosic Fibres by FTIR Spectroscopy - Thread and Single Fibre Analysis by Attenuated Total Reflectance," *Stud. Conserv.*, vol. 48, no. 4, pp. 269–275, Dec. 2003.

[82]    M. L. Nelson and R. T. O'Connor, "Relation of certain infrared bands to cellulose crystallinity and crystal latticed type. Part I. Spectra of lattice types I, II, III and of amorphous cellulose," *J. Appl. Polym. Sci.*, vol. 8, no. 3, pp. 1311–1324, May 1964.

[83]    *Structure Determination of Organic Compounds*. Berlin, Heidelberg: Springer Berlin Heidelberg, 2009.

[84]    S. Suganuma *et al.*, "Hydrolysis of Cellulose by Amorphous Carbon Bearing SO 3 H, COOH, and OH Groups," *J. Am. Chem. Soc.*, vol. 130, no. 38, pp. 12787–12793, Sep. 2008.

[85]    C. Qiao, G. Chen, J. Zhang, and J. Yao, "Structure and rheological properties of cellulose nanocrystals suspension," *Food Hydrocoll.*, vol. 55, pp. 19–25, Apr. 2016.

[86]    M. Börjesson, K. Sahlin, D. Bernin, and G. Westman, "Increased thermal stability of nanocellulose composites by functionalization of the sulfate groups on cellulose

nanocrystals with azetidinium ions," *J. Appl. Polym. Sci.*, vol. 135, no. 10, p. 45963, Mar. 2018.

[87] M. Cao *et al.*, "Direct exfoliation of graphite into graphene in aqueous solutions of amphiphilic peptides," *J. Mater. Chem. B*, vol. 4, no. 1, pp. 152–161, 2016.

[88] J. I. Paredes, S. Villar-Rodil, A. Martínez-Alonso, and J. M. D. Tascón, "Graphene Oxide Dispersions in Organic Solvents," *Langmuir*, vol. 24, no. 19, pp. 10560–10564, Oct. 2008.

[89] Y. Zhou, Q. Bao, L. A. L. Tang, Y. Zhong, and K. P. Loh, "Hydrothermal Dehydration for the 'Green' Reduction of Exfoliated Graphene Oxide to Graphene and Demonstration of Tunable Optical Limiting Properties," *Chem. Mater.*, vol. 21, no. 13, pp. 2950–2956, Jul. 2009.

[90] R. Abdullah, K. Ueda, and S. Saka, "Hydrothermal decomposition of various crystalline celluloses as treated by semi-flow hot-compressed water," *J. Wood Sci.*, vol. 60, no. 4, pp. 278–286, Aug. 2014.

[91] Beck, "Auto-catalyzed acidic desulfation of cellulose nanocrystals," *Nord. Pulp Pap. Res. J.*, vol. 29, no. 01, pp. 006–014, Mar. 2014.

[92] J. S. Foos, "Synthesis and Characterization of Semiconductive Poly-1,4-Dimethoxybenzene and Its Derived Polyquinone," *J. Electrochem. Soc.*, vol. 133, no. 4, p. 836, 1986.

[93] D. Häringer, "Poly(5-amino-1,4-naphthoquinone), a Novel Lithium-Inserting Electroactive Polymer with High Specific Charge," *J. Electrochem. Soc.*, vol. 146, no. 7, p. 2393, 1999.

[94] T. Le Gall, K. H. Reiman, M. C. Grossel, and J. R. Owen, "Poly(2,5-dihydroxy-1,4-benzoquinone-3,6-methylene): a new organic polymer as positive electrode material for rechargeable lithium batteries," *J. Power Sources*, vol. 119–121, pp. 316–320, Jun. 2003.

[95] K. Liu, J. Zheng, G. Zhong, and Y. Yang, "Poly(2,5-dihydroxy-1,4-benzoquinonyl sulfide) (PDBS) as a cathode material for lithium ion batteries," *J. Mater. Chem.*, vol. 21, no. 12, p. 4125, 2011.

[96] Z. Song, Y. Qian, T. Zhang, M. Otani, and H. Zhou, "Poly(benzoquinonyl sulfide) as a High-Energy Organic Cathode for Rechargeable Li and Na Batteries," *Adv. Sci.*, vol. 2, no. 9, p. 1500124, Sep. 2015.

[97] L. Sieuw, B. Ernould, J.-F. Gohy, and A. Vlad, "On the improved electrochemistry of hybrid conducting-redox polymer electrodes," *Sci. Rep.*, vol. 7, no. 1, p. 4847, Dec. 2017.

[98] G. Socrates, *Infrared and Raman Characteristic Group Frequencies: Tables and Charts*, 3rd ed. John Wiley & Sons, 2004.

[99] M. W. Sabaa, T. M. Madkour, and A. A. Yassin, "Polymerization products of p-Benzoquinone as bound antioxidants for styrene-butadiene rubber: Part I—Preparation of quinone polymers," *Polym. Degrad. Stab.*, vol. 22, no. 3, pp. 195–203, Jan. 1988.

[100] T. M. Madkour, "Chemistry of Polymerization Products of p-Benzoquinone. 13C NMR and Molecular Dynamics Study," *Polym. J.*, vol. 29, no. 8, pp. 670–677, Aug. 1997.

[101] J. C. Meyer, "Transmission electron microscopy (TEM) of graphene," in *Graphene*, Elsevier, 2014, pp. 101–123.

[102] P. S. Guin, S. Das, and P. C. Mandal, "Electrochemical Reduction of Quinones in Different Media: A Review," *Int. J. Electrochem.*, vol. 2011, pp. 1–22, 2011.